TU Delft

Delft University of Technology

Large eddy simulations of reacting and non-reacting transcritical fuel sprays using multiphase thermodynamics

Fathi, Mohamad; Hickel, Stefan; Roekaerts, Dirk

DOI
10.1063/5.0099154

Publication date
2022

Document Version
Final published version

Published in
Physics of Fluids

Citation (APA)
Fathi, M., Hickel, S., & Roekaerts, D. (2022). Large eddy simulations of reacting and non-reacting transcritical fuel sprays using multiphase thermodynamics. *Physics of Fluids*, *34*(8), Article 085131. https://doi.org/10.1063/5.0099154

Important note
To cite this publication, please use the final published version (if applicable).
Please check the document version above.

Copyright
Other than for strictly personal use, it is not permitted to download, forward or distribute the text or part of it, without the consent of the author(s) and/or copyright holder(s), unless the work is under an open content license such as Creative Commons.

Takedown policy
Please contact us and provide details if you believe this document breaches copyrights.
We will remove access to the work immediately and investigate your claim.

This work is downloaded from Delft University of Technology.
For technical reasons the number of authors shown on this cover page is limited to a maximum of 10.

Physics of Fluids

Large eddy simulations of reacting and non-reacting transcritical fuel sprays using multiphase thermodynamics

Cite as: Phys. Fluids **34**, 085131 (2022); https://doi.org/10.1063/5.0099154
Submitted: 15 May 2022 • Accepted: 25 July 2022 • Accepted Manuscript Online: 25 July 2022 • Published Online: 18 August 2022

Published open access through an agreement with Delft University of Technology

Mohamad Fathi, Stefan Hickel and Dirk Roekaerts

COLLECTIONS

Paper published as part of the special topic on Development and Validation of Models for Turbulent Reacting Flows

This paper was selected as Featured

View Online Export Citation CrossMark

ARTICLES YOU MAY BE INTERESTED IN

Multiscale analysis of the Reynolds stress, dissipation, and subgrid-scale tensor in turbulent bubbly channel flows: Characterization of anisotropy and modeling implications
Physics of Fluids **34**, 085122 (2022); https://doi.org/10.1063/5.0104594

Orientation dynamics of anisotropic and polydisperse colloidal suspensions
Physics of Fluids **34**, 083317 (2022); https://doi.org/10.1063/5.0101702

Computational study of inertial migration of prolate particles in a straight rectangular channel
Physics of Fluids **34**, 082021 (2022); https://doi.org/10.1063/5.0100963

Physics of Fluids
Special Topic: Hydrogen Flame and Detonation Physics
Submit Today!

AIP Publishing

© 2022 Author(s).

Physics of Fluids ARTICLE scitation.org/journal/phf

Large eddy simulations of reacting and non-reacting transcritical fuel sprays using multiphase thermodynamics

Cite as: Phys. Fluids **34**, 085131 (2022); doi: 10.1063/5.0099154
Submitted: 15 May 2022 · Accepted: 25 July 2022 ·
Published Online: 18 August 2022

View Online Export Citation CrossMark

Mohamad Fathi,[1] Stefan Hickel,[1,a)] and Dirk Roekaerts[2]

AFFILIATIONS

[1]Aerodynamics Group, Faculty of Aerospace Engineering, Technische Universiteit Delft, Kluyverweg 2, 2629 HT Delft, The Netherlands
[2]Process and Energy, Faculty of Mechanical, Maritime and Materials Engineering, Technische Universiteit Delft, Leeghwaterstraat 39, 2628 CB Delft, The Netherlands

Note: This paper is part of the special topic, Development and Validation of Models for Turbulent Reacting Flows.
[a)]**Author to whom correspondence should be addressed:** S.Hickel@tudelft.nl

ABSTRACT

We present a novel framework for high-fidelity simulations of inert and reacting sprays at transcritical conditions with highly accurate and computationally efficient models for complex real-gas effects in high-pressure environments, especially for the hybrid subcritical/supercritical mode of evaporation during the mixing of fuel and oxidizer. The high-pressure jet disintegration is modeled using a diffuse interface method with multiphase thermodynamics, which combines multi-component real-fluid volumetric and caloric state equations with vapor–liquid equilibrium calculations for the computation of thermodynamic properties of mixtures at transcritical pressures. Combustion source terms are evaluated using a finite-rate chemistry model, including real-gas effects based on the fugacity of the species in the mixture. The adaptive local deconvolution method is used as a physically consistent turbulence model for large eddy simulation (LES). The proposed method represents multiphase turbulent fluid flows at transcritical pressures without relying on any semi-empirical breakup and evaporation models. All multiphase thermodynamic model equations are presented for general cubic state equations coupled with a rapid phase-equilibrium calculation method that is formulated in a reduced space based on the molar specific volume function. LES results show a very good agreement with available experimental data for the reacting and non-reacting engine combustion network benchmark spray A at transcritical operating conditions.

© 2022 Author(s). All article content, except where otherwise noted, is licensed under a Creative Commons Attribution (CC BY) license (http://creativecommons.org/licenses/by/4.0/). https://doi.org/10.1063/5.0099154

I. INTRODUCTION

In-depth understanding of turbulent reacting multiphase flows at transcritical pressures is essential for the design and optimization of efficient energy conversion systems, such as liquid rocket engines, or modern diesel engines and gas turbines. Such systems typically require the rapid injection of cold liquid or liquid-like supercritical fuels into a chamber environment with an elevated pressure and temperature. Combustion occurs after transcritical evaporation during mixing of the fuel with a hot and pressurized gas or gas-like supercritical oxidizer. The term *transcritical* refers to an operating pressure higher than the critical pressure of the pure fuel or oxidizer streams, but lower than the cricondenbar pressures of their possible mixtures. Since the cricondenbar point of hydrocarbon/air mixtures is unreachable even at elevated pressures of several hundred bars, the operating pressure of most energy conversion systems is transcritical in practice.

Although the operating conditions are often nominally supercritical with respect to the fuel stream and a direct transition from a liquid to a gas-like supercritical state is expected, aligned with Gibbsian thermodynamics and experimental reports,[1–4] the mixture can locally enter the two-phase regime and interfaces between liquid-like and gas-like phases may form. Transcritical jets and sprays, therefore, resemble a combination of the classical two-phase disintegration with breakup and evaporation of droplets and the supercritical turbulent mixing of two dense fluids. This hybrid behavior complicates their numerical simulation; despite comprehensive experimental campaigns, it is not

© Author(s) 2022

well understood which type of the jet disintegration dominates under exactly which conditions.

Traditional large eddy simulation (LES) of the high-speed transcritical injection have either modeled the transcritical multiphase fluid flows by Lagrangian particle tracking (LPT) methods with sharp vapor–liquid interfaces,[5–7] or by Eulerian single-phase dense-gas (DG) approaches with diffuse vapor–liquid interfaces.[8–10] LES-LPT and LES-DG approaches are efficient for many flows, but their inherent model assumptions impose significant limitations at transcritical conditions. The standard LPT method is very sensitive to empirical tuning parameters and was developed for dilute mixtures, neglecting real-fluid effects. The LES-DG approach, on the other hand, excludes transcritical phase separation and may lead to nonphysical or ill-defined states when a part of the flow passes the metastable boundaries, in particular, at lower transcritical pressures.[11] Furthermore, some important transcritical effects such as the high solubility of the saturated liquids or the different evaporation rates of the components of the fuel are not captured by these models; see also the discussion in Refs. 12–16, for example.

Using multiphase thermodynamics (MT) in the context of a diffuse-interface method has been demonstrated recently to be a promising technique to overcome the aforementioned limitations.[14,17] In this formulation, the fully conservative Navier–Stokes equations (NSE) are solved for a hypothetical multi-component fluid mixture with thermo-transport properties computed using a suitable equation of state (EOS) coupled with vapor–liquid equilibrium (VLE) calculations. Although the weak surface tension force is neglected, the method can accurately capture the flow physics including the subcritical region of coexisting multi-component vapor and liquid as well as the non-ideal fluid behavior such as dissolution of the ambient gas in the compressed liquid.

LES-MT studies show excellent agreement with experimental data for the non-reacting transcritical sprays;[14,18,19] however, the applicability of the method to reacting flows remained as an open question mainly due to the high computational cost of the VLE calculations, which increases with the number of components in the mixture, and due to the need for chemistry models that can capture the departure from ideal-gas (IG) behavior in regions with high pressures and low temperatures. The latter can be solved using an appropriate reduced reaction mechanism[20] and utilizing the fugacity values of species in the mixture for the evaluations of real fluid effects on the reaction rates.[21]

The non-ideal fluid behavior becomes apparent when using an appropriate EOS. Two-parameter cubic EOS, such as the Soave–Redlich–Kwong (SRK)[22] and Peng–Robinson (PR)[23] models, are very popular because of their computational efficiency.[17,24–27] The intrinsic drawback of these two-parameter cubic EOS is the use of a universal critical compressibility factor, which can severely limit their accuracy close to the critical point. To overcome this limitation, volume translation methods can be employed to improve the density predictions, but the calculation of consistent caloric properties is computationally very expensive and, thus, simplified approximations are typically used in practice.[28] Another option is utilizing a cubic EOS with three parameters. The Redlich–Kwong–Peng–Robinson (RKPR) model of Cismondi and Mollerup[29] calibrates the cubic EOS using the actual value of the compressibility at the critical point and provides a consistent framework for real-fluid thermodynamic modeling at tractable computational cost.[30]

To alleviate the high computational cost of VLE calculations of reacting fluids, which typically have a very large number of components, Fathi and Hickel[31] have recently introduced a new phase-splitting method, which is formulated in a reduced space and based on the molar specific values of the volume function. In comparison with the conventional method (e.g., Refs. 14 and 32), the reduction method prevents the quadratic growth of the computational time with the number of components. The formulation based on the volume function leads to a robust and quick convergence near the critical point and phase boundaries. In addition, the novel method is directly applicable to isoenergetic–isochoric conditions aligned with the transported variables in conservative compressible Navier–Stokes flow solvers. Combined, this yields a very considerable speed-up for the simulation of transcritical flows with many components.[31]

In this paper, we present several novel physical and numerical models that improve the accuracy and computational efficiency of high-fidelity simulation of turbulent reacting and non-reacting multiphase flows at transcritical pressures. The framework is provided by a fully conservative formulation of the multi-component compressible Navier–Stokes equations with multiphase thermodynamics models and the adaptive local deconvolution method (ALDM) for LES turbulence modeling.[33] Improved accuracy compared to previous LES-MT simulations is provided by the RKPR EOS[29] for transcritical vaporization and real-fluid properties, and by fugacity-based finite rate chemistry for combustion modeling. The computational cost is significantly reduced by a rapid VLE solver,[31] which uses reduction methods for the phase-splitting calculations, and by utilizing a highly optimized reaction mechanism,[20] which reduces the required number of transported species. The proposed LES-MT method is validated by comparing computational results with experimental data reported for the transcritical reacting and non-reacting engine combustion network (ECN) spray-A benchmark test cases.

II. PHYSICAL AND NUMERICAL MODELS

We use the LES-MT method for solving reacting multiphase compressible Navier–Stokes equations in a fully conservative form with real-fluid thermo-transport properties and fugacity-based finite-rate chemistry. In this section, the required physical and numerical models for the MT-based simulations are presented.

A. Governing equations

The three-dimensional compressible reacting Navier–Stokes equations (NSE) describe the conservation of mass, species, momentum, and total (absolute) internal energy,

$$\partial_t \rho + \nabla \cdot (\rho \mathbf{u}) = 0, \tag{1}$$

$$\partial_t \rho Y_i + \nabla \cdot (\rho Y_i \mathbf{u}) = \nabla \cdot \mathbf{j}_i + \dot{\omega}_i, \tag{2}$$

$$\partial_t \rho \mathbf{u} + \nabla \cdot (\rho \mathbf{u}\mathbf{u} + p\mathbf{I}) = \nabla \cdot \boldsymbol{\tau}, \tag{3}$$

$$\partial_t \rho e_t + \nabla \cdot [(\rho e_t + p)\mathbf{u}] = \nabla \cdot (\mathbf{u} \cdot \boldsymbol{\tau} - \mathbf{q}), \tag{4}$$

where ρ is the mixture mass density, $\mathbf{u}$ is the velocity vector, p is the thermodynamic pressure of the mixture, and $e_t = e + |\mathbf{u}|^2/2$ is the total absolute specific internal energy of the mixture and e is the corresponding absolute specific internal energy. For species $i = 1, 2, \ldots, N$ with N being the total number of components comprising the mixture, Y_i is the mass fraction, $\mathbf{j}_i$ is the diffusive mass-flux vector, and $\dot{\omega}_i$ is the net mass production rate. $\boldsymbol{\tau}$ and $\mathbf{q}$ denote the viscous stress tensor and

© Author(s) 2022

the vector of heat fluxes. $\mathbf{I}$ is the unit tensor and ∇ is the nabla operator.

The viscous stress tensor is modeled by assuming a Newtonian fluid and Stokes' hypothesis,

$$\boldsymbol{\tau} = \mu\left(\nabla\mathbf{u} + (\nabla\mathbf{u})^T\right) - 2/3\mu(\nabla\cdot\mathbf{u})\mathbf{I}. \tag{5}$$

The molecular viscosity coefficient μ of the multi-component mixture is estimated using Chung's correlations.[34] We neglect bulk-viscosity effects in our computations because accurate models to be used at pressures close to the critical point are unavailable.

For multi-component fluid flows, the total heat flux vector,

$$\mathbf{q} = -\lambda\nabla T - \sum_{i=1}^{N} h_i\mathbf{j}_i\,, \tag{6}$$

consists of heat conduction and interspecies enthalpy diffusion, and is a function of the thermal conductivity of the mixture λ, temperature T, and the partial mass absolute enthalpy h_i of component i. Similar to the viscosity, the thermal conductivity of the mixture is modeled by Chung's correlations.[34]

By neglecting Soret and Dufour effects, the mass diffusion $\mathbf{j}_i$ is modeled using Fick's law through a simplified correlation based on the mixture averaged diffusion approximation along with an extra term to ensure zero total mass diffusion,

$$\mathbf{j}_i = \rho D_i\nabla Y_i - Y_i\sum_{j=1}^{N}\rho D_j\nabla Y_j. \tag{7}$$

The effective binary diffusion coefficient between species i and the bulk mixture is approximated by

$$\rho D_i = (1 - X_i)\Big/\sum_{j\neq i}^{N} X_j/(\rho D_{ij}), \tag{8}$$

where X_i is the mole fraction of species i, which can be computed via $X_i = Y_i M/M_i$ from the mass fractions and the mean molecular weight $M = 1/(\sum_i^N Y_i/M_i)$ of the mixture, with M_i being the molar mass of the species i. The product of density and the binary mass diffusion coefficient of species i and j, ρD_{ij}, can be approximated accurately with Chapman and Enskog theory[34] without high-pressure corrections if the system pressure is under 100 bar.[35]

B. Multiphase thermodynamics

Simulations of multi-component fluid flows at elevated pressure require proper volumetric and caloric EOS that account for the volume of molecules and interactive forces between them in order to accurately calculate pressure and temperature from the density, internal energy, and mass composition of the mixture. The partial mass enthalpies of all components in the mixture are additionally required for the evaluation of the interspecies enthalpy diffusion flux. At transcritical pressures, additional phase-splitting calculation should be carried out to account for the coexistence of vapor and liquid phases. In this section, we present the equations required for the computation of temperature, pressure, and partial mass enthalpies of a general fluid in single phase or two phases in equilibrium.

1. Volumetric equation of state

A volumetric EOS represents the thermodynamic relation between the pressure, specific volume (inverse of the density), and temperature of a single-phase substance that can be pure or a multi-component mixture. The most popular volumetric EOS is the ideal gas (IG); however, its applicability is limited to gaseous media with a compressibility factor close to unity, that is, it is only appropriate at relatively high temperatures and low pressures. For the typical pressures and temperatures of transcritical fuel sprays, cubic EOS are an attractive compromise between accuracy, model complexity, and computational cost.

The most widely used cubic EOS are SRK[22] and PR.[23] Both are formulated based on two model parameters. They have the intrinsic limitation of predicting a unique and universal compressibility factor at the critical point, which therefore results in a systematic error for the specific volume (or density) at conditions close to the critical point. To overcome this limitation, Cismondi and Mollerup[29] proposed a three-parameter cubic EOS. This so-called RKPR EOS considers the effect of the actual critical compressibility factor as the third EOS parameter. In Fig. 1, we compare the accuracy of various cubic EOS against the highly accurate reference EOS of Lemmon and Huber[36] for pure n-dodecane at the ECN spray A operating pressure 60 bar. The data show that RKPR EOS significantly improves on the known deficiencies of two-parameter EOS (SRK and PR). The RKPR EOS can also yield more accurate predictions of caloric properties than the perturbed chain-statistical associating fluid theory (PC-SAFT) EOS,[37] such as shown for the heat capacity in the temperature range $450 \leq T \leq 750$ K in Fig. 1. The advantages of using the RKPR EOS for the prediction of the fluid properties at the transcritical and supercritical pressures have also been highlighted previously.[14,30,38]

The RKPR EOS is employed for all application examples discussed in the present paper. However, as the general cubic EOS,

$$p = \mathcal{R}T/(\bar{\vartheta} - b) - a/[(\bar{\vartheta} + \delta_1 b)(\bar{\vartheta} + \delta_2 b)]\,, \tag{9}$$

includes IG, SRK, PR, RKPR, and other EOS as special cases, all thermodynamic model relations are presented in form of this general cubic EOS, in which $\mathcal{R}$ is the universal gas constant, $\bar{\vartheta} = M/\rho$ is the molar specific volume, a is the attractive energy parameter, and b is the co-volume parameter. δ_1 and δ_2 are two constant parameters in the case of two-parameter cubic EOS, whereas they are variables computed from one extra constraint in the case of three-parameter cubic EOS. With the RKPR EOS, the energy parameter is

$$a = (3\xi^2 + 3\xi d + d^2 + d - 1)/ (3\xi + d - 1)^2(\mathcal{R}^2T_c^2/p_c)[3/(2 + T/T_c)]^m, \tag{10}$$

where $d = (1 + \delta_1^2)/(1 + \delta_1)$, $\xi = 1 + [2(1 + \delta_1)]^{\frac{1}{3}} + [4/(1 + \delta_1)]^{\frac{1}{3}}$, and

$$m = (-2.4407\mathcal{Z}_c + 0.0017)\omega^2 + (7.4513\mathcal{Z}_c + 1.9681)\omega + (12.5040\mathcal{Z}_c - 2.7238), \tag{11}$$

with $\mathcal{Z}_c = 1.168Z_c$ being the tuned critical compressibility factor. The co-volume parameter of the RKPR EOS is

$$b = (\mathcal{R}T_c/p_c)/(3\xi + d - 1). \tag{12}$$

The third parameter,

© Author(s) 2022

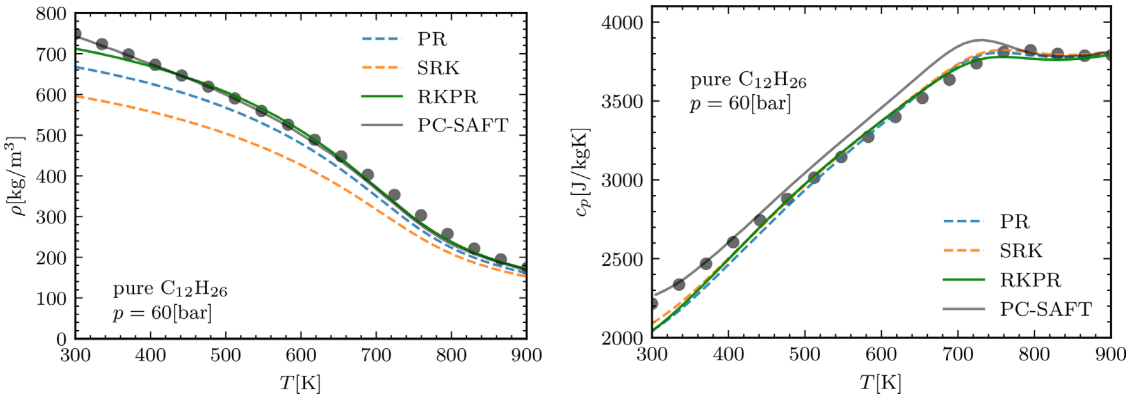


FIG. 1. Density (left) and constant-pressure heat capacity (right) of pure n-dodecane predicted by PC-SAFT,[37] PR,[23] SRK,[22] and RKPR[29] compared with the reference EOS of Lemmon and Huber[36] denoted by circles.

$$\delta_1 = 0.428 + 18.496(0.338 - \mathcal{Z}_c)^{0.66} + 789.723(0.338 - \mathcal{Z}_c)^{2.512}, \tag{13}$$

is an empirical function of $\mathcal{Z}_c$, and δ_2 follows from the constraint,

$$\delta_2 = (1 - \delta_1)/(1 + \delta_1). \tag{14}$$

In these equations, p_c, T_c, Z_c, and ω are the critical pressure, critical temperature, critical compressibility factor, and acentric factor of the pure fluid.

The conventional approach to extend this pure-fluid cubic EOS to multi-component mixtures is based on considering the mixture as a pure hypothetical substance and estimating the EOS parameters via the van der Waals mixing rule,

$$\begin{aligned} a &= \sum_{i=1}^{N}\sum_{j=1}^{N} X_i X_j a_{ij}, \\ b &= \sum_{i=1}^{N} X_i b_i, \\ \delta_1 &= \sum_{i=1}^{N} X_i \delta_{1,i}, \\ \delta_2 &= \sum_{i=1}^{N} X_i \delta_{2,i}, \end{aligned} \tag{15}$$

where a_{ij} is obtained through a combination rule that can include any possible binary interaction effects among the components. We use the classical combination rule,

$$a_{ij} = (1 - \varrho_{ij})(a_i a_j)^{\frac{1}{2}}, \tag{16}$$

with ϱ_{ij} being the binary interaction coefficient between components i and j in the mixture. In contrast to the pseudo-critical combination rule, in which a_{ij} is estimated by the pure-fluid formula of the energy parameter with critical quantities estimated based on those for components i and j, the classical combination rule (16) provides the possibility of applying reduction methods for the phase equilibrium calculations, which can significantly reduce the computational costs for mixtures with many components. Using the reduction theory,[31] the energy parameter of the mixture can be computed through

$$a = \sum_{k=1}^{N_m} \lambda_k q_k^2 \quad \text{where } q_k \equiv \sum_{i=1}^{N} X_i s_{ki} a_i^{\frac{1}{2}}. \tag{17}$$

Here, λ_k and s_{ki} are significant (non-zero) eigenvalues and their corresponding eigenvectors for a symmetric matrix with entries $\varrho'_{ij} = 1 - \varrho_{ij}$. N_m is the number of significant eigenvalues. More often than not, binary interaction coefficients are set to zero due to lack of accurate data or just to simplify the computations. In that case, the matrix of ϱ'_{ij} becomes a diagonal matrix, and $N_m = 1$ regardless of the number of components in the mixture.

a. Single-phase pressure. The RKPR EOS explicitly provides the thermodynamic pressure of a thermodynamically stable mixture whose molar composition, specific volume, and temperature are specified. The required temperature is computed via the caloric EOS, which is explained in Sec. II B 2 for non-ideal multi-component fluids.

2. Caloric equation of state

A caloric EOS provides a thermodynamic relation between a caloric property like specific internal energy, and two other properties such as temperature and specific volume for a mixture with specified molar or mass composition. Real-fluid caloric EOS can be derived by the departure function formalism using the volumetric EOS. For the general cubic EOS (9), the molar specific internal energy $\bar{e} = Me$ of a multi-component real fluid is obtained as follows:

$$\begin{aligned} \bar{e} = \sum_{i=1}^{N} X_i \bar{h}_i^{\circ}(T) - \mathcal{R}T + (a - T\partial a/\partial T)/ \\ [(\delta_2 - \delta_1)b] \ln\left[(\bar{v} + \delta_1 b)/(\bar{v} + \delta_2 b)\right], \end{aligned} \tag{18}$$

where the first two terms account for the absolute internal energy of the mixture at the actual temperature but at the standard pressure, and the last term accounts for the internal energy change via an isothermal thermodynamic path from the standard reference pressure to the actual value.

The molar specific enthalpy at standard pressure is usually computed using polynomials,[39]

© Author(s) 2022

$$\bar{h}_i^\circ(T)/\mathcal{R} = -A_{i,1}/T + A_{i,2}\ln T + \sum_{j=1}^{5} A_{i,j+2}T^j/j + A_{i,8}, \quad (19)$$

where $A_{i,1\ldots8}$ are the calibrated polynomial coefficients for each component i, which include the formation enthalpy.

a. Single-phase temperature. The temperature of a stable mixture with specified molar composition, molar specific volume, and molar specific internal energy is determined implicitly via the caloric Eq. (18). It can be computed numerically by an initial guess and Newton iterations,

$$T = T^* - \mathcal{L}(\bar{e} - \bar{e}^*)/\bar{c}_V^*, \quad (20)$$

where $\mathcal{L}$ is the line search parameter in order to ensure global convergence, $\bar{e}$ is the target energy, and $\bar{e}^*$ is computed via Eq. (18) using T^*. Here, $\bar{c}_V^*$ is the molar specific heat capacity at constant volume and computed at temperature T^*. The thermodynamic relation required for the evaluation of $\bar{c}_V$ using the departure function formalism for a general cubic EOS is

$$\bar{c}_V = \sum_{i=1}^{N} X_i \bar{c}_{P,i}^\circ(T) - \mathcal{R} + T\partial^2 a/\partial T^2[(\delta_1 - \delta_2)b] \times \ln\left[(\bar{\vartheta} + \delta_1 b)/(\bar{\vartheta} + \delta_2 b)\right]. \quad (21)$$

The specific molar heat capacity of the component i at the standard pressure is computed by taking the derivative of the polynomial (19) with respect to the temperature, which yields

$$\bar{c}_{P,i}^\circ(T)/\mathcal{R} = \sum_{j=1}^{7} A_{i,j}T^{j-3}. \quad (22)$$

3. Vapor–liquid equilibrium

When vapor and liquid phases coexist, phase-splitting calculations are necessary in order to correctly determine the thermodynamic properties of the multi-component mixture, of which overall values of molar specific internal energy $\bar{e}$, molar specific volume $\bar{\vartheta}$, and molar composition X_i are known. The required phase-splitting or flash calculations are briefly explained in this section.

The two-phase equilibrium state of a fluid with N components is described by N equations for species mass conservation and $2 + N$ equations for temperature, pressure, and species chemical potentials of the two phases. This set of $2N + 2$ equations must be supplemented with two more constraints in order to uniquely determine the molar specific volume, temperature, and molar composition of the multi-component liquid and vapor phases. These two constraints define the type of the flash problem. As we solve the conservative form of the governing Navier–Stokes equations, that is, transport equations for the mixture energy and density, isoenergetic–isochoric phase-splitting calculations, also known as UV-flash calculations, must be carried out. The two additional constraints for UV-flash calculations are

$$\bar{\vartheta} = (1 - \alpha)\bar{\vartheta}_l + \alpha\bar{\vartheta}_v \quad (23)$$

and

$$\bar{e} = (1 - \alpha)\bar{e}_l + \alpha\bar{e}_v. \quad (24)$$

Subscripts l and v refer to liquid and vapor values, and α is the vapor mole fraction, defined as the ratio of the mole of the vapor phase to the total mole of all phases. In order to evaluate the required specific internal energies of the liquid and vapor phases, we use Eq. (18) for each phase separately, and to compute α, we use the total mass balance rewritten as follows:

$$\alpha = (M - M_l)/(M_v - M_l), \quad (25)$$

with M as overall average molecular weight computed using overall mole fractions X_i. M_l and M_v are the average molecular weights for the liquid and vapor mixtures that are computed from the liquid mole fractions $X_{l,i}$ and vapor mole fractions $X_{v,i}$, respectively. The molar compositions of liquid and vapor phases represent the solution of the phase-splitting calculations.

In order to solve the flash equations more efficiently, Fathi and Hickel[31] recently introduced a new method that performs UV-flash calculations very fast and robust via Newton iterations with the exact Jacobian of the equilibrium temperature used for VT-flash calculations. The VT-flash here refers to isochoric–isothermal phase-splitting calculations, which this method formulates in an effectively reduced space in terms of the molar specific value of the volume function of Mikyška and Firoozabadi[40] and reduced parameters similar to those used by Nichita and Graciaa.[41] In the following, we briefly explain how this method can be used to determine the equilibrium temperature and pressure in a general cubic EOS framework. For a comprehensive review and practical implementation guidelines, interested readers are referred to the original paper.[31]

a. Equilibrium temperature. The temperature in the two-phase region is obtained through an iterative method similar to that used for the single-phase case, but using the specific vapor and liquid internal energies and heat capacities to determine the overall values,

$$\bar{e}^* = (1 - \alpha)\bar{e}_l^* + \alpha\bar{e}_v^*, \quad \bar{c}_V^* = (1 - \alpha)\bar{c}_{V,l}^* + \alpha\bar{c}_{V,v}^*. \quad (26)$$

Vapor and liquid quantities require the molar composition and specific volume of that phase, which are the results of the rapid VT-flash calculations together with the vapor mole fraction. The iterative method can be terminated when $|\bar{e} - \bar{e}^*|/|\bar{e}| < 10^{-6}$.

According to Fathi and Hickel,[31] the VT-flash problem can be formulated based on effective reduced parameters $\vec{\mathcal{H}} = (\mathcal{H}_1^\Delta, \ldots, \mathcal{H}_{N_m+2}^\Delta)$ derived from Helmholtz free energy using species molar specific volume functions. The reduced parameters are determined iteratively by applying the Newton–Raphson method for $N_m + 2$ error equations,

$$\mathcal{E}_k \equiv \mathcal{H}_{k,v}(\vec{\mathcal{H}}) - \mathcal{H}_{k,l}(\vec{\mathcal{H}}) - \mathcal{H}_k^\Delta = 0, \quad (27)$$

for $k = 1, \ldots, N_m + 2$ with the Jacobian matrix,

$$\mathcal{J}_{kj} \equiv \frac{\partial \mathcal{E}_k}{\partial \mathcal{H}_j^\Delta} = \frac{\partial \mathcal{H}_{k,v}}{\partial \mathcal{H}_j^\Delta} - \frac{\partial \mathcal{H}_{k,l}}{\partial \mathcal{H}_j^\Delta} - \delta_{kj}, \quad (28)$$

for $k, j = 1, \ldots, N_m + 2$. In order to compute $\vec{\mathcal{H}}_v$ and $\vec{\mathcal{H}}_l$ as well as the required partial derivatives analytically, we first compute the K-factors,

© Author(s) 2022

$$\ln \mathcal{K}_i = \sum_{k=1}^{N_m} \mathcal{H}_k^{\Delta} s_{ki} + \mathcal{H}_{N_m+1}^{\Delta} b_i + \mathcal{H}_{N_m+2}^{\Delta}, \tag{29}$$

with $\mathcal{K}_i \equiv y_i/x_i$ being the K-factor of the component i in the mixture. Afterward, the vapor mole fraction is initially obtained by the solving the classic Rachford–Rice equation,

$$\sum_{i=1}^{N} [X_i(\mathcal{K}_i - 1)]/[1 + \alpha(\mathcal{K}_i - 1)] = 0. \tag{30}$$

Next, the vapor and liquid molar compositions are obtained from the material balances and the K-factors through

$$\begin{aligned} X_{i,l} &= X_i/[1 + \alpha(\mathcal{K}_i - 1)], \\ X_{i,v} &= X_{i,l}\mathcal{K}_i \end{aligned} \tag{31}$$

for $i = 1, 2, \ldots, N$. From the molar compositions for both phases, we compute the required parameters of the RKPR EOS, including $a, q, b, \delta_1, \delta_2$ through the relations given in Sec. II B 1 for a stable single-phase mixture. The specific molar volume of the vapor is then evaluated through the isochoric constraint,

$$\bar{\vartheta}_v = \left[\bar{\vartheta} - (1 - \alpha)\bar{\vartheta}_l\right]/\alpha. \tag{32}$$

Requiring equality of pressures between two phases, the liquid specific molar volume for the general cubic EOS is the solution of a fifth-order polynomial,

$$\varsigma_5 \bar{\vartheta}_l^5 + s_4 \bar{\vartheta}_l^4 + \varsigma_3 \bar{\vartheta}_l^3 + \varsigma_2 \bar{\vartheta}_l^2 + \varsigma_1 \bar{\vartheta}_l + \varsigma_0 = 0. \tag{33}$$

The polynomial coefficients $\varsigma_{0..5}$ are listed in Ref. 31. They are functions of the parameters that we computed in the previous steps. Finally, $\mathcal{H}_{k,l}$ or $\mathcal{H}_{k,v}$ is computed from

$$\mathcal{H}_k = 2\lambda_k q_k \ln\left[(\bar{\vartheta} + \delta_1 b)/(\bar{\vartheta} + \delta_2 b)\right]/[(\delta_1 - \delta_2) b \mathcal{R}T], \tag{34}$$

for $k \le N_m$,

$$\begin{aligned} \mathcal{H}_k = a/(\mathcal{R}Tb^2)\{&\bar{\vartheta} b/\left[(\bar{\vartheta} + \delta_1 b)(\bar{\vartheta} + \delta_2 b)\right] \ldots \\ &-\ln\left[(\bar{\vartheta} + \delta_1 b)/(\bar{\vartheta} + \delta_2 b)\right]/(\delta_1 - \delta_2)\} - (v - b)^{-1} \end{aligned} \tag{35}$$

for $k = N_m + 1$ and

$$\mathcal{H}_k = \ln(\bar{\vartheta} - b), \tag{36}$$

for $k = N_m + 2$. Note that the subscripts l and v are dropped for simplicity as these equations apply to both phases. The required equations are listed in Ref. 31 including the analytical expression of the components of the Jacobian matrix.

Starting the procedure requires an initial guess for the vector $\vec{\mathcal{H}} = (\mathcal{H}_1^{\Delta}, \ldots, \mathcal{H}_{N_m+2}^{\Delta})$. This can be calculated from K-factor values by following the steps from the solution of the Rachford–Rice until the evaluation of $\mathcal{H}_{k,l}$ and $\mathcal{H}_{k,v}$. Then, the vector of reduced parameters can be computed using its definition via

$$\mathcal{H}_k^{\Delta} = \mathcal{H}_{k,v} - \mathcal{H}_{k,l} \tag{37}$$

for $k = 1, \ldots, N_m + 2$. Typically, the K-factors are available from previous time steps in computational fluid dynamics simulations. In the case of blind flashes, where no previous equilibrium information is available, one can use Wilson's correlation as an initial guess.

b. Equilibrium pressure. Neglecting the surface tension force, the pressure is equal for both phases in equilibrium. As we used this equality for the determination of specific volumes, the equilibrium pressure is the saturation pressure of vapor or liquid obtained by the flash calculations at the equilibrium temperature.

4. Partial enthalpy

By definition, the partial derivative of a quantity with respect to the mole fraction of a species while keeping temperature, pressure, and mole fractions of the other species unchanged is called the partial molar value of that quantity. It can be shown that thermodynamic relations between extensive quantities are also valid for corresponding partial values. In this section, the calculation of the partial (mass) enthalpy in the multiphase thermodynamics framework is briefly explained, as it is required for the heat flux (6) and for some discretization schemes.

The (mass-basis) partial enthalpies can be computed easily from the mole-basis ones: $h_i = \bar{h}_i/M_i$. The partial molar enthalpy for a single-phase mixture with known temperature, specific volume, and molar composition can be computed via the thermodynamic relation,

$$\bar{h}_i = \bar{e}_i + p\bar{\vartheta}_i, \tag{38}$$

where $\bar{\vartheta}_i \equiv (\partial\bar{\vartheta}/\partial X_k)|_{T,P,X_{j\neq k}}$ is the partial molar volume, which can be obtained from its definition for the considered volumetric EOS (9) as follows:

$$\begin{aligned} \bar{\vartheta}_i = -\{&\mathcal{R}T/(\bar{\vartheta} - b) + \mathcal{R}Tb_i/(\bar{\vartheta} - b)^2 \ldots \\ &+ ab_i\left[2b\delta_1\delta_2 + \bar{\vartheta}(\delta_1 + \delta_2)\right]/\left[(\bar{\vartheta} + \delta_1 b)(\bar{\vartheta} + \delta_2 b)\right]^2 \ldots \\ &- a_i/\left[(\bar{\vartheta} + \delta_1 b)(\bar{\vartheta} + \delta_2 b)\right]\}/(\partial p/\partial\bar{\vartheta})|_{T,X_j}, \end{aligned} \tag{39}$$

where $a_i \equiv (\partial a/\partial X_i)|_{T,P,X_{j\neq i}}$ can be computed using reduced parameters,[31]

$$a_i = -2\left(\sum_{k=1}^{N_m} \lambda_k q_k s_{ki} a_i^{1/2}\right), \tag{40}$$

and

$$\begin{aligned} (\partial p/\partial\bar{\vartheta})|_{T,X_j} = &-\mathcal{R}T/(\bar{\vartheta} - b)^2 + a\left[2\bar{\vartheta} + (\delta_1 + \delta_2)b\right]/ \\ &\left[(\bar{\vartheta} + \delta_1 b)(\bar{\vartheta} + \delta_2 b)\right]^2. \end{aligned} \tag{41}$$

The partial molar internal energy $\bar{e}_i \equiv (\partial\bar{e}/\partial X_k)|_{T,P,X_{j\neq k}}$ can be computed from the caloric EOS as follows:

$$\begin{aligned} \bar{e}_i = &\bar{h}_i^{\circ}(T) - \mathcal{R}T + (\bar{\vartheta}_i - \bar{\vartheta} b_i/b)(a - T\partial a/\partial T)/ \\ &\left[(\bar{\vartheta} + \delta_1 b)(\bar{\vartheta} + \delta_2 b)\right] \ldots \\ &+ \left[T(b_i\partial a/\partial T - b\partial a_i/\partial T) + ba_i - ab_i\right] \\ &\times \ln\left[(\bar{\vartheta} + \delta_1 b)/(\bar{\vartheta} + \delta_2 b)\right]/\left[(\delta_2 - \delta_1)b^2\right]. \end{aligned} \tag{42}$$

Note that we have neglected the dependence of δ_1 and δ_2 on the molar composition in the above proposed equations following the approach used by Gmehling *et al.*[42] for SRK and PR EOS.

a. Equilibrium partial enthalpy. If the mixture is unstable in a single phase, then phase-equilibrium calculations are necessary in order

© Author(s) 2022

to determine the thermodynamic properties of a stable mixture of saturated vapor and liquid phases. The overall partial enthalpy of the component i can then be estimated as follows:

$$X_i\bar{h}_i \simeq (1-\alpha)X_{i,l}\bar{h}_{i,l} + \alpha X_{i,v}\bar{h}_{i,v}. \tag{43}$$

C. Real finite-rate chemistry

Chemical reactions change the composition of a fluid mixture via the formation and destruction of species, which is expressed in the species mass balance equations by net mass production rates $\dot{\omega}_i$. At elevated pressures, finite-rate chemistry models have to account for the non-ideal thermodynamic state. Differences from the usually used ideal-gas definitions are addressed in this section.

Similar to the mass action law of the elementary reactions, the species net mass production rates of reactions with non-integer stoichiometric coefficients can also be expressed as follows:

$$\dot{\omega}_i = M_i \sum_{r=1}^{N_r} (\nu_{ir}^{\mathcal{P}} - \nu_{ir}^{\mathcal{R}}) \mathcal{Q}_r, \tag{44}$$

where N_r is the total number of reactions, and $\nu_{ir}^{\mathcal{P}}$ and $\nu_{ir}^{\mathcal{R}}$ are the positive molar stoichiometric coefficients of species i on the right (product) and left (reactant) side of the reaction r, which might be non-integer numbers in general. The reaction rate $\mathcal{Q}_r$ of the reaction r depends on the concentrations of the reactants through

$$\mathcal{Q}_r = k_{f,r} \prod_{j=1}^{N} \mathcal{C}_j^{n'_{jr}} - k_{b,r} \prod_{j=1}^{N} \mathcal{C}_j^{n''_{jr}}. \tag{45}$$

The forward and backward rate coefficients k_{fr} and k_{br} are usually expressed by the Arrhenius law,

$$k(T) = \mathcal{A} \exp\left[-E_a/(\mathcal{R}T)\right], \tag{46}$$

as an exponential function of the temperature, with $\mathcal{A}$ being the pre-exponential factor and E_a the reaction activation energy. In addition, n'_{jr} and n''_{jr} are reaction orders with respect to species j in the forward and backward reactions. Reaction orders might be listed separately for global reactions; otherwise, they are considered equal to the molar stoichiometric coefficients of that species in the reactants and products.

It is important to note that the concentrations $\mathcal{C}_j$ of the species j in Eq. (44) should be computed in a thermodynamically consistent way for dense gaseous mixtures at high pressure. We propose to use the species' fugacity for this purpose, that is,

$$\mathcal{C}_j \simeq f_j/(\mathcal{R}T), \tag{47}$$

with f_j being the fugacity of species j in the mixture. The fugacity is computed from the fugacity coefficient $\varphi_j = f_j/(X_j p)$, which can be obtained using the molar specific volume function,

$$\varphi_j = \mathcal{R}T/(p\psi_j), \tag{48}$$

with ψ_j being the molar specific value of volume function for species j (see Ref. 31). Using the definition of the fugacity coefficient and the molar specific volume function, the required concentration can, therefore, be computed via the following simple relation for non-ideal multi-component gases:

$$\mathcal{C}_j = X_j/\psi_j, \tag{49}$$

where ψ_j can be computed using the effective reduced parameters,

$$\ln\psi_j = \sum_{k=1}^{N_m} \mathcal{H}_k s_{kj} + \mathcal{H}_{N_m+1} b_j + \mathcal{H}_{N_m+2} \tag{50}$$

with $\mathcal{H}_1, \ldots, \mathcal{H}_{N_m+2}$ computed using the gas or supercritical mixture temperature, composition, and specific volume via Eqs. (34)–(36). Note that in the limit of very high temperature, the fugacity coefficient tends toward unity and the ideal-gas mixture formula $\mathcal{C}_j = X_j p/(\mathcal{R}T)$ is recovered consistently.

The fugacity-based evaluation of concentrations via Eq. (47) simplifies the computation of the backward reaction coefficient whenever it is not explicitly provided. In such cases, the backward rate coefficient should be computed using the equilibrium constant $K_c = k_f/k_b$. If the reaction rates are expressed as proposed in terms of the fugacity, the equilibrium constant can be computed similarly to the ideal-gas formula in Ref. 43 from

$$K_{c,r} = [p^\circ/(\mathcal{R}T)]^{\nu_r} \exp\left[\Delta S_r^\circ/\mathcal{R} - \Delta H_r^\circ/(\mathcal{R}T)\right], \tag{51}$$

with $\nu_r = \sum_{i=1}^{N} (\nu_{ir}^{\mathcal{P}} - \nu_{ir}^{\mathcal{R}})$ being the net change in the number of species in the reaction, and ΔH_r° and ΔS_r° being the reaction enthalpy and entropy net change at the standard pressure $p^\circ = 1$ atm.

D. Large eddy simulation

In this work, LES is utilized for turbulence modeling. LES provides the time-accurate evolution of the large scales of fluid flows that encompass almost all of the mechanical energy of the turbulent fluid motion. The evolution of the large scales is governed by a coarse-grained or low-pass filtered form of the Navier–Stokes equations. The effect of nonlinear interactions between the large resolved scales and the small truncated ones is taken into account via an appropriate modeling of the subgrid-scale (SGS) stress tensor.

In explicit LES, the SGS tensor is approximated based on the continuous filtered differential equations and model expression depending on, e.g., the filtered strain rate and possibly other quantities for which additional transport equations are needed, and the discretization of the continuous filtered transport and model equations in space and time is carried out afterward using standard approximation theory. For implicit LES, however, the coarse-grained discrete numerical model is directly derived in a single approximation step that includes models for the effects of unresolved interactions consistent with a specifically tailored high-order numerical discretization.[44]

The LES presented in this paper have been performed with the adaptive local deconvolution method (ALDM) of Hickel *et al.*,[33] which is a physically consistent implicit LES method based on a nonlinear, solution adaptive finite-volume discretization scheme and spectral turbulence theory. ALDM is appropriate for LES of the full Mach number range without any user-defined model parameters. Its superior performance in comparison with common explicit LES models has been reported by Müller *et al.*[45] for several transcritical and supercritical nitrogen jets. As discussed by Matheis and Hickel,[14] ALDM does not account for all additional SGS quantities that appear after low-pass filtering the non-linear equations used for the evaluation of the thermo-transport properties and chemistry sources in transcritical flows. Although novel ideas toward modeling some of these terms have been proposed, their performance for transcritical conditions at high

© Author(s) 2022

Reynolds number remains unclear due to a lack of experimental data for high-order statistics and spatial details. ALDM has been extensively verified and validated for transcritical injector flows; for example, by Matheis *et al.*[28] for Tani's cryogenic coaxial injector, by Müller *et al.*[46] for Oschwald's coaxial injector, and by Matheis and Hickel[14] for the non-reacting ECN spray-A.

E. Numerical implementation

Real-fluid multiphase thermodynamics and the fugacity-based finite rate chemistry model are implemented in our fluid flow solver INCA (https://www.inca-cfd.com). We employ the same discretization schemes for the transport equations as Matheis and Hickel.[14] In this subsection, these schemes are briefly reviewed.

The governing equations are discretized in space by a conservative finite-volume scheme that uses a second-order central difference method for the diffusion terms, and ALDM for the inviscid fluxes. The van Albada limiter[47] is utilized for the mass and energy flux reconstruction to avoid spurious oscillations with possible under- or overshoots at sharp density gradients.

A second-order Strang-splitting scheme is utilized to separate the stiff chemical reactions from the advection and diffusion mechanisms. The method consists of three major steps: First, the solution is updated by considering only the reaction source terms in half a time step by means of a stiff ODE solver. We used VODE[48] for this purpose, which is a variable-coefficient implicit solver based on fifth-order backward differentiation formulas. Second, the obtained solution is set as initial condition for a full advection and diffusion time step with the explicit third-order strong stability preserving Runge–Kutta scheme of Gottlieb and Shu.[49] Finally, the solution is updated with the second half reaction step. The time step size is adapted dynamically according to the Courant–Friedrichs–Lewy stability condition with CFL = 1.

III. CASE STUDY: TRANSCRITICAL ECN SPRAY-A

A. Experimental setups

The standard reacting and non-reacting test cases of ECN spray-A[50] are selected for validation and demonstration. The fuel is pure n-dodecane ($C_{12}H_{26}$) with a low temperature of 363 K and is injected into a chamber with a pressure of 60 bar and a temperature of 900 K. At these conditions, the cold liquid n-dodecane undergoes a transcritical vaporization process, since the chamber pressure is much higher than the critical pressure (18.2 bar) of n-dodecane. The injection rail pressure is 1500 bar, and the injector consists of a hydro-eroded single-hole nozzle with the nominal diameter of $D = 0.09$ mm, leading to the injection of about 3.5 mg of n-dodecane fuel with a relatively constant jet velocity of about 600 ms^{-1} during the injection time of about 1.5 ms. The chamber gas is mostly nitrogen, to which oxygen is added for the reacting case. Elevated concentrations of carbon dioxide and water vapor result from burning acetylene along with hydrogen in the preparation stage. Table I summarized the initial molar composition of the gas in the chamber.

TABLE I. Mole percentage of species in the chamber of reacting and non-reacting cases.

	O_2	N_2	CO_2	H_2O
Non-reacting	0.00	89.71	6.52	3.77
Reacting	15.00	75.15	6.23	3.62

B. Computational setup

1. Grid specifications

All simulations have been carried out using a mesh generated for a three-dimensional rectangular domain with a length of 934 D in the axial direction and 467 D in the lateral directions, with $D = 0.09$ mm being the nominal diameter of the injector nozzle.

To minimize the total number of computational cells, we instruct the flow solver INCA to perform static zonal mesh refinement within a user-define region of interest. This region of interest is defined as a 10° cone that encloses the injected jet. The target level of refinement inside the cone is defined based on the distance from the injector nozzle, with resolution steps at axial locations 665, 411, 254, 157, 97 and 60 D from the injector nozzle. The resulting mesh is shown in Fig. 2. The multi-block structured grid consists of 2864 blocks and 12.7×10^6 cells with seven resolution levels, which are marked by L1–L7 in Fig. 2. Around 40% of the cells belong to the finest level with $\Delta y_{min} = \Delta z_{min} \simeq 10.25\,\mu$m and $\Delta x_{min} = 2\Delta y_{min}$ located in the near-nozzle region ($x/D < 60$); see the zoomed area on the left side in the figure.

2. Boundary conditions

The injector nozzle is not resolved; instead, a suitable transient inflow condition is used at the injector's nozzle exit plane. This inflow is pure n-dodecane at a temperature of 363 K and a pressure of 60 bar with a transient axial velocity that provides the same amount of momentum as the experiment. We calculated the mass flow rate with the CMT virtual injection rate generator (http://www.cmt.upv.es) with input parameters according to the experimental conditions and a fuel density of 687.24 kg m^{-3} consistent with the RKPR EOS at the given pressure and temperature. Figure 3 shows the generated transient injection velocity. Subsonic inlet conditions are used as the Mach number of the pure liquid is approximately 0.5 at the nozzle exit. Mass densities and the velocity vector are imposed as Dirichlet boundary condition and a homogeneous Neumann condition is used for the static pressure. The transient profile is directly used as boundary condition without adding any artificial turbulent fluctuations at the boundary. The induced shear and hydrodynamic pressure fluctuations at 600 ms^{-1} are expected to be strong enough to create turbulence almost instantaneously.

Subsonic pressure outflow conditions are imposed at the exit face, with a constant static pressure of 60 bar as Dirichlet condition and extrapolation of the other independent flow variables from the domain inside. Adiabatic no-slip conditions are applied for all other boundaries of the rectangular domain.

3. Reaction mechanism

The finite-rate chemistry model formulated for the real-fluid effects in Sec. II C is used for the calculation of chemical source terms in the species mass conservation equations. To alleviate the already high computational load of the LES-MT method, the highly reduced global two-step reaction mechanism of Hakim *et al.*[51] is selected. This mechanism was calibrated using Bayesian inference for the precise

© Author(s) 2022

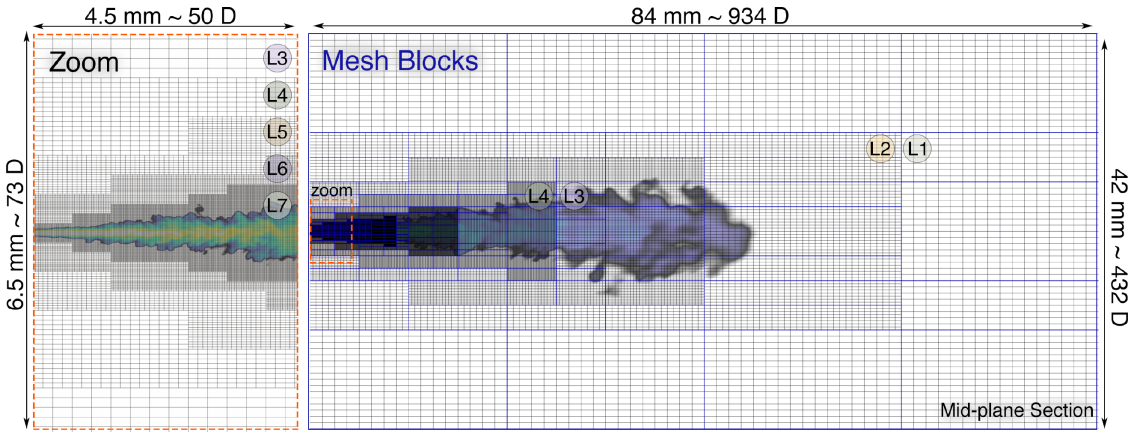


FIG. 2. A mid-plane section of the 3D multi-block structured grid with seven levels of mesh refinements generated for LES-MT of reacting and non-reacting ECN spray-A.

prediction of the ignition delay time of n-dodecane combustion at the experimental condition of the ECN spray-A test case.[51] The reduced mechanism has six species. Similar to the approach of Westbrook and Dryer for the oxidation of paraffins, the incomplete oxidation of n-dodecane is accounted for by two-step reactions as given below:

$$C_{12}H_{26} + 12.5O_2 \rightarrow 12CO + 13H_2O, \tag{52}$$

$$CO + 0.5O_2 \rightleftharpoons CO_2. \tag{53}$$

The forward reaction rates (in cgs units) are expressed in Arrhenius form,

$$\mathcal{Q}_1 = \mathcal{A}_1 \exp\left[-31944/(\mathcal{R}T)\right]\mathcal{C}_{C_{12}H_{26}}^{0.25}\mathcal{C}_{O_2}^{1.25}, \tag{54}$$

$$\mathcal{Q}_2 = 3.98 \times 10^{14} \exp\left[-40\,000/(\mathcal{R}T)\right]\mathcal{C}_{CO}\mathcal{C}_{H_2O}^{0.5}\mathcal{C}_{O_2}^{0.25} \cdots - 5 \times 10^{8} \exp\left[-40\,000/(\mathcal{R}T)\right]\mathcal{C}_{CO_2}. \tag{55}$$

The logarithm of the Arrhenius pre-exponential factor of the first reaction varies according to the local fresh-gas condition dynamically through

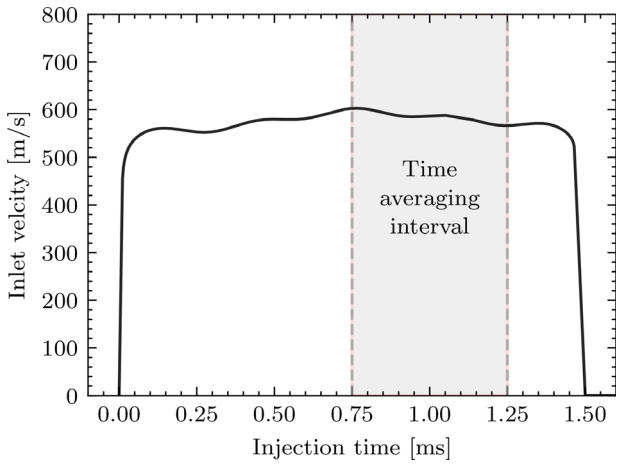


FIG. 3. Transient injection velocity profile used for the simulation of reacting and non-reacting ECN spray-A test cases, computed for using RKPR EOS.

$$\ln \mathcal{A}_1 = \theta_0 + \theta_1 \exp\left(\theta_2\phi_0\right) + \theta_3 \tanh[(\theta_4 + \theta_5\phi_0)T_0 + \theta_6]. \tag{56}$$

The best possible values of θ_0–θ_6 found by matching the ignition delay time with the skeletal mechanism of Narayanaswamy *et al.*[52] are listed in Table II. The local fresh gas temperature T_0 and equivalence ratio ϕ_0 can be estimated using the local value of mixture fraction.[9] The mixture fraction is computed here by tracking the inert nitrogen mass fraction,

$$f = (Y_{N_2}^{ox} - Y_{N_2})/Y_{N_2}^{ox}, \tag{57}$$

with $Y_{N_2}^{ox} = 0.72$ in the oxidizer stream of reacting case.

We evaluate the performance of the reduced two-step six-species reaction mechanism of Hakim *et al.*[20] by calculating the ignition delay time in a homogeneous constant-volume reactor for a stoichiometric mixture of the fuel and oxidizer of the reacting spray-A case. The volume of the reactor is set according to the initial temperature, stoichiometric composition, and pressure of 60 bar using the RKPR EOS. Table III lists the critical values and the acentric factor of the species required for the simulations of ECN spray-A with this reduced reaction mechanism. Figure 4 shows the time elapsed until the temperature of the reactor has increased by 400 K above its initial value. We observe an excellent agreement between the ignition delay time predicted by the reduced two-step mechanism used in this study and the skeletal mechanism of Narayanaswamy *et al.*[52] with 876 reactions and 164 species.

IV. NUMERICAL RESULTS

In this section, we use the experimental reference data of the reacting and non-reacting ECN spray-A in order to evaluate and validate the proposed multiphase thermodynamics and real-fluid finite rate chemistry model for transcritical fuel sprays.

TABLE II. The optimal parameters for evaluation of the pre-exponential factor of n-dodecane reaction in the reduced mechanism of Hakim *et al.*[51]

θ_0	θ_1	θ_2	θ_3	θ_4	θ_5	θ_6
27.38	−2.13	−2.05	1.89	−0.01	2.87×10^{-4}	8.43

© Author(s) 2022

TABLE III. Critical properties and acentric factor of the species.

Species	T_c (K)	p_c (bar)	Z_c (−)	ω (−)
$C_{12}H_{26}$	658.0	18.20	0.251	0.576
O_2	154.6	50.43	0.288	0.022
N_2	126.2	34.00	0.289	0.038
CO_2	304.2	73.83	0.274	0.224
H_2O	647.1	220.6	0.229	0.345
CO	132.9	34.99	0.299	0.048

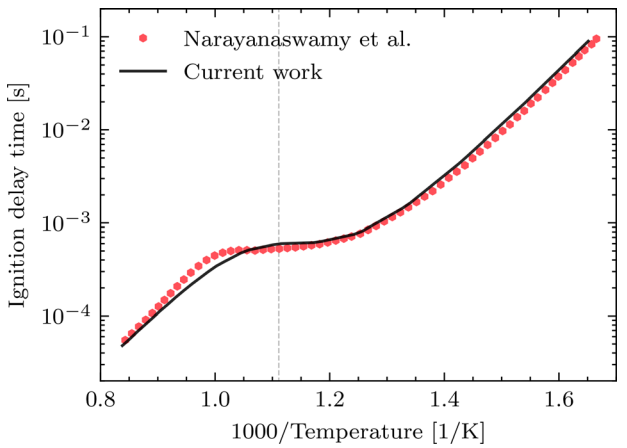


FIG. 4. Ignition delay time for the skeletal mechanism of Narayanaswamy *et al.*[52] and the current work using the reduced mechanism of Hakim *et al.*[20] for the stoichiometric mixture of the fuel and oxidizer of ECN spray-A.

A. Non-reacting case

We compare the experimental and numerical flow visualizations of the inert spray-A at seven specific instants after the start of injection (ASOI) in Fig. 5. The left column shows experimental schlieren images,[53] and the right column shows predictions of our LES-MT model. The non-reacting jet first penetrates in axial direction and spreads in radial direction while evaporating and mixing with the hot chamber gas, and then maintains an approximately constant radius after some downstream distance from the injector nozzle. In the experimental schlieren images, the saturated dark regions represent the liquid phase. For LES-MT snapshots, we show colored contours of the liquid volume fraction (LVF), which also indicate the amount of the liquid phase, and density gradients in the single-phase gaseous regions, where LVF = 0. The liquid penetration length (LPL) is reported to be about 10 mm in the experiment, which is in excellent agreement with our numerical results (see also Fig. 6).

Figure 6 shows the temporal evolution of the liquid penetration length (LPL) and the vapor penetration length (VPL) for the LES-MT numerical simulation and experimental measurements.[54,55] For the LES-MT, LPL and VPL are defined as the maximum axial locations with a LVF of 15% and a mixture fraction of 0.01%, respectively, similar to in previous studies.[17] The LPL signals of LES and experiment are in excellent agreement. For the VPL, we observe excellent match up to about 0.6 ms. At later times, the simulation predicts slightly larger values than those measured in the experiment. This could be due to the coarsened mesh at those locations far from the nozzle, or due to measurement uncertainties. The estimated uncertainty of the experimental measurements is indicated by the gray-shaded area and significantly increases with time. On the right side of the same figure, we also compare an experimental snapshot with highlighted liquid and vapor boundaries with a numerical visualization. The agreement is good, considering that both snapshots are instantaneous samples of independent realizations of highly turbulent flows.

We present the ensemble averaged profiles of the mixture fraction on the centerline and at two downstream locations in Fig. 7. The statistics have been computed by ensemble averaging LES data collected at eight circumferential sections every 0.5 μs during the time interval highlighted in Fig. 3. LES-MT results follow the measured axial profiles very well. At the first station, $x = 18$ mm, the n-dodecane mass fraction on the jet axis is overestimated by the LES compared to the experiment; however, the LES data fully agrees with the experimental data further downstream, which can be also seen from the radial profiles at $x = 36$ mm.

Figure 8 shows global scatter plots of the temperature and the mole fractions of the major species n-dodecane and nitrogen as a function of the mixture fraction. Each point represents an instantaneous local state of the resolved LES-MT flow field for the non-reacting case at 680 μs. The data points are colored with the molar vapor fraction in a way that green is completely vapor and purple is completely liquid. The two-phase region at the nominal operating pressure of 60 bar is indicated in the temperature/mixture-fraction diagram. A hypothetical temperature profile predicted by multiphase thermodynamics assuming isenthalpic mixing at 60 bar is also shown. Two-phase boundary and isenthalpic curve cross each other at a mixture fraction of about 0.34 for this case using RKPR EOS. The LES data points follow the isenthalpic line strikingly well. This is explained in more detail in Refs. 14 and 17. In the two phase region, liquid and vapor phases have different molar composition, as determined by phase-equilibrium computations. The vapor and liquid compositions are shown for the two major species, n-dodecane and nitrogen, in the mole-fraction/mixture-fraction diagrams in Fig. 8. The diagrams indicate that the saturated liquid contains only about 90% n-dodecane and the rest is mostly nitrogen. This is a consequence of the high solubility of nitrogen in n-dodecane at transcritical pressures and questions the standard pure-fuel assumption made for liquid droplets in traditional LPT methods.

Figure 9 shows contours of the molar composition of the overall mixture as well as the compositions of the liquid and vapor phases for all species. The figure indicates the spatial evolution of mixing process controlled by multiphase thermodynamics. While the heavy n-dodecane molecules represent about 90% of the total moles of the liquid core, they are in minority in the vapor phase, which consists mainly of light nitrogen molecules corresponding to the initial composition of the chamber gas. The fuel-rich liquid core extends up to about 3 mm from the injector nozzle. Far from the nozzle and close to the tip of the liquid core, where the vapor mole fraction is close to unity, the mixture composition is close to the saturated vapor phase and, accordingly, the mixture fraction is close to 0.34. Water has roughly the same concentration in the liquid and vapor phases, which is in contrast to nitrogen, n-dodecane, and carbon dioxide. This means that water in

© Author(s) 2022

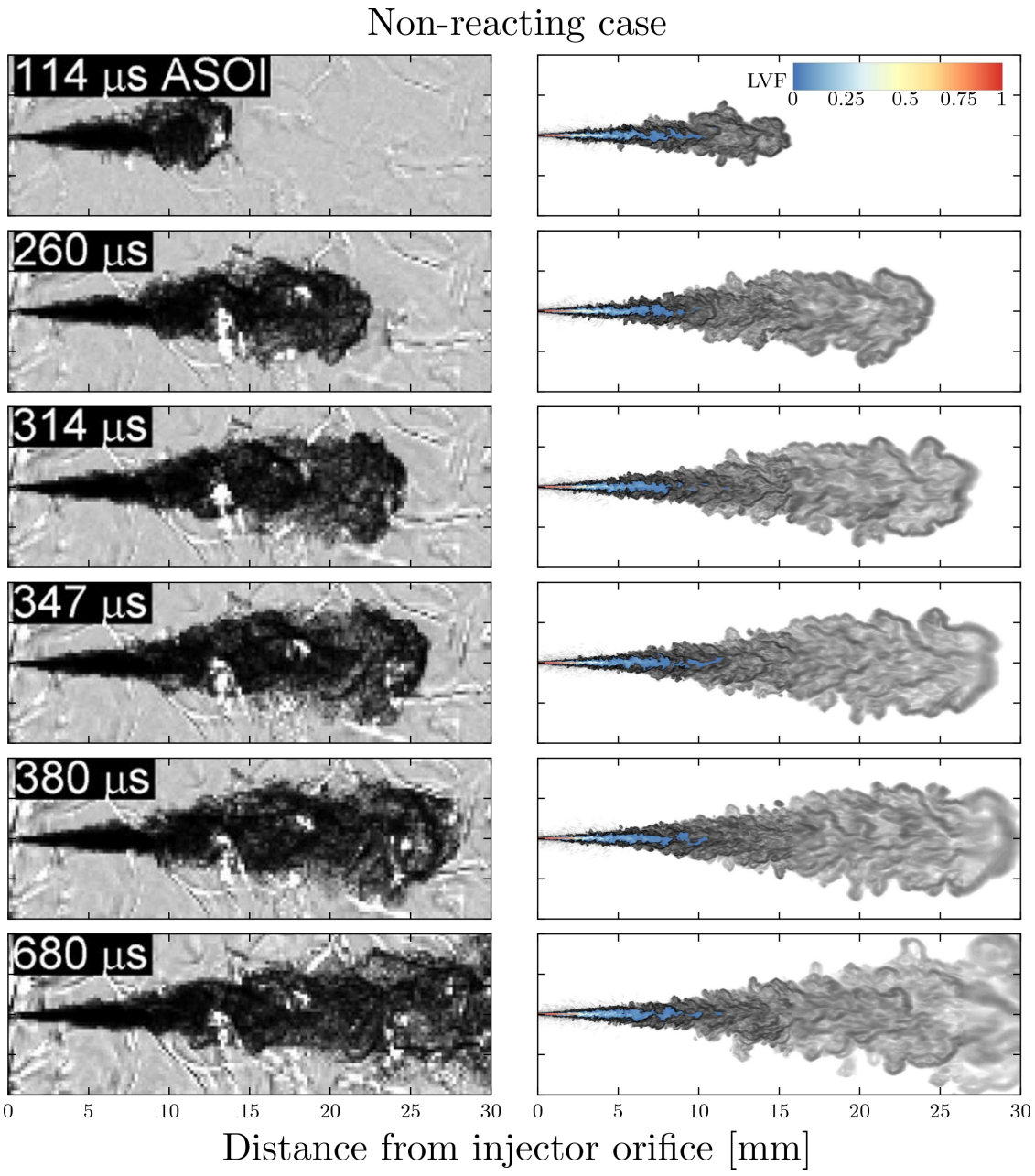


FIG. 5. Schlieren images of the non-reacting spray-A (left: experiment[53]) and density gradient contours of LES-MT solution, overprinted in the two-phase region by liquid volume fraction contours (right).

contact with the cold n-dodecane dissolves quickly into the liquid phase, while the other species in the environment mostly stay in the saturated vapor phase.

B. Reacting case

The temporal evolution of the reacting ECN spray-A is shown in Fig. 10. This figure shows experimental schlieren images[53] on the left side and corresponding snapshots of the LES-MT solution on the right side. Similar to the inert test case, the liquid phase appears as a saturated black region in the experimental schlieren images and contours of the LVF show the predicted amount of liquid for the LES-MT. There is a very good agreement between the experiment and simulation, and the jet develops very similar to inert spray up to the autoignition. The ignition delay time is approximately 400 μs for both experiment and simulation. Around the ignition time, low-temperature reactions are activated in a significant portion of the

© Author(s) 2022

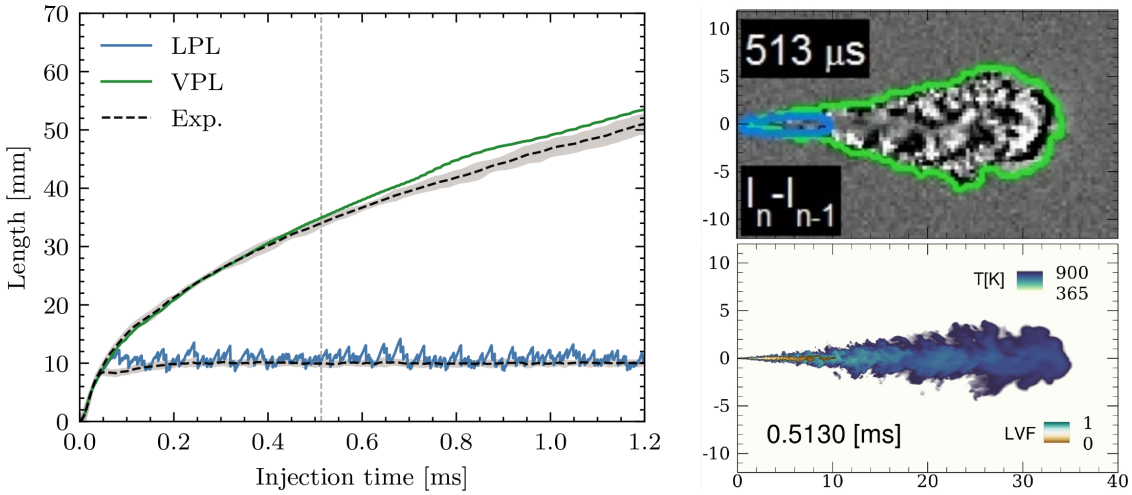


FIG. 6. Vapor and liquid penetration trajectories for LES-MT and experiment[54,55] for the non-reacting ECN spray-A on the left, and an experimental schlieren image with highlighted vapor and liquid boundaries compared with an LES-MT temperature contour overprinted with LVF in the liquid and two-phase region at the same instance on the right.

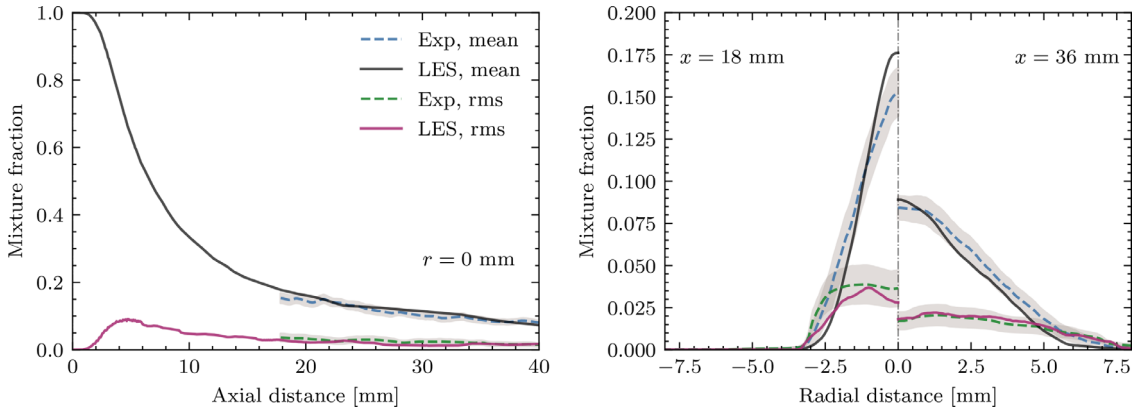


FIG. 7. Axial (left) and radial (right) profiles of mean and RMS fluctuations of the mixture fraction computed using LES-MT method in comparison with Rayleigh scattering measurements[56] for the non-reacting spray-A.

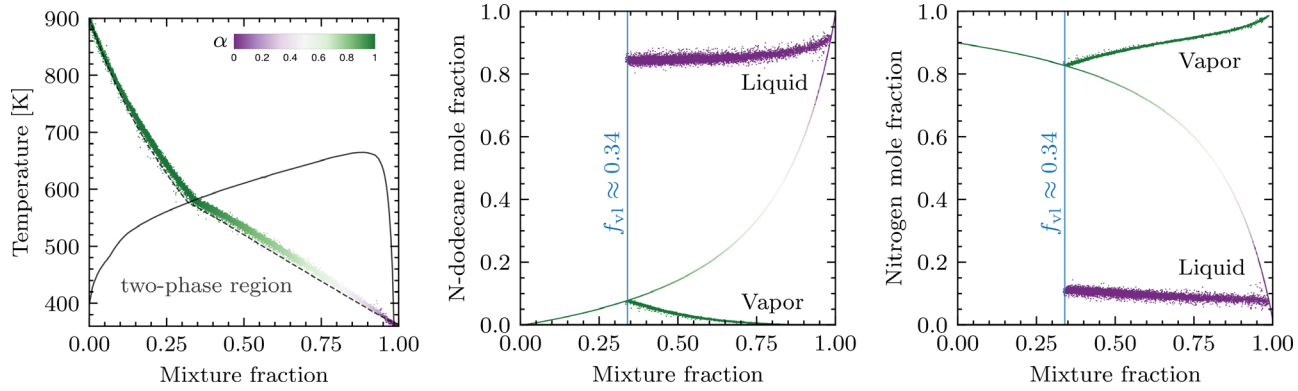


FIG. 8. Scatter plots of the LES results for the non-reacting spray-A at 680 μs colored by vapor mole fraction values. The temperature/mixture-fraction diagram (left) shows also the temperature variation during an isenthalpic process (dashed line) and two phase region boundaries at 60 bar. The n-dodecane (middle) and nitrogen (right) mole fraction diagrams show the overall as well as the saturated liquid and vapor phases.

© Author(s) 2022

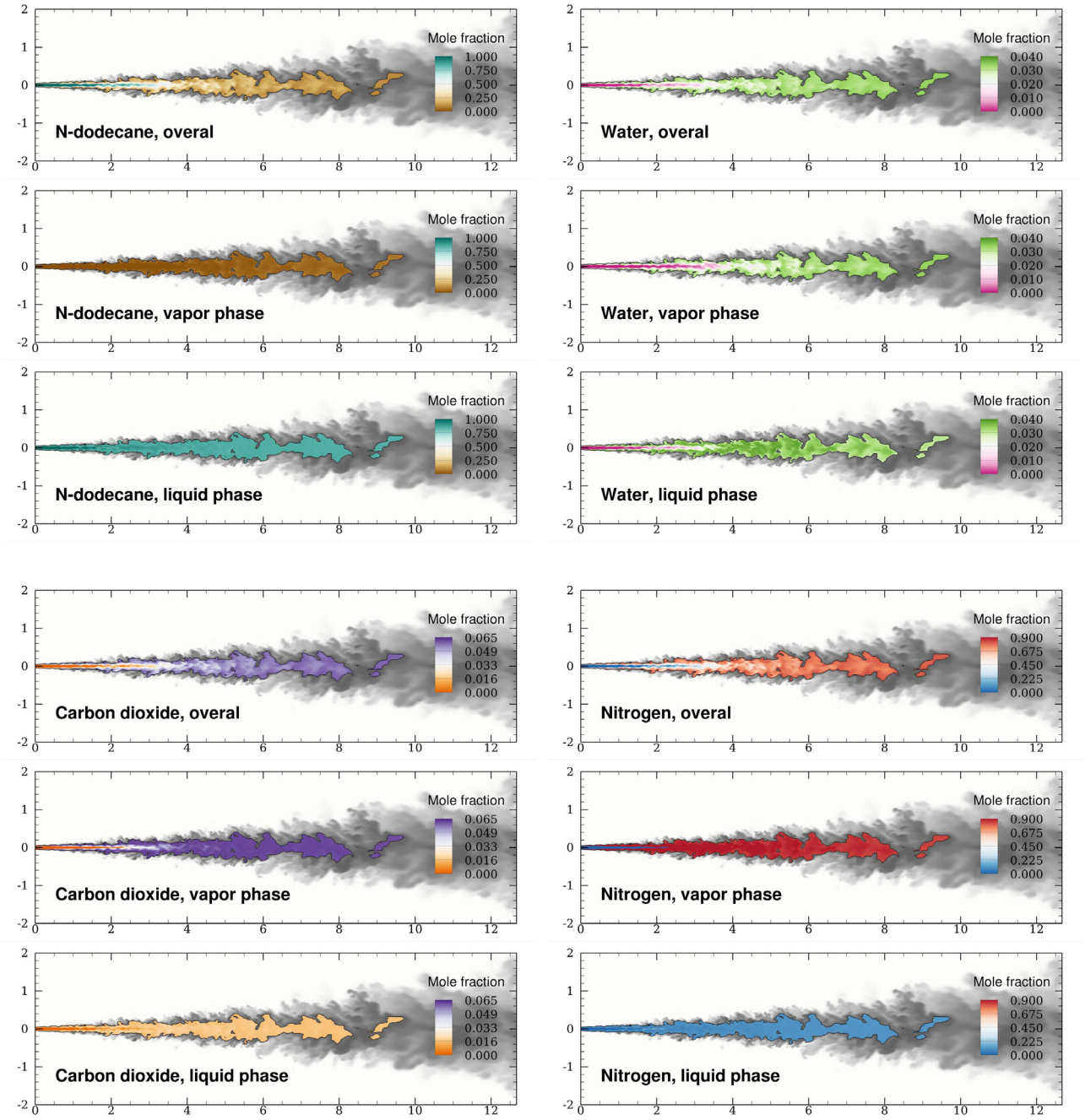


FIG. 9. Instantaneous molar composition of the overall fluid, as well as the composition of the vapor and liquid phases. The background contour represents the temperature field from dark to light shades. In the two-phase region, contours of the species mole fraction of saturated liquid, saturated vapor, and overall mixture are presented.

vaporized fuel. This is detectable between 20 and 25 mm after 314 μs via brighter regions in the schlieren images and visualized by blue iso-temperature surfaces at 920 K for the LES-MT results. The high-temperature ignition occurs after the low-temperature reactions created a sufficient concentration of radicals and intermediate species. The highly reacting region is highlighted by the red iso-temperature surface at 2000 K for the LES results in the last snapshot at 680 μs. The high-temperature ignition is a rapid volumetric process. An abrupt radial expansion of the reacting jet, compared to the inert case, is observed near the location of the flame front. We observe good agreement of the experimental flame liftoff length (LOL) with our LES-MT result which is about 15 mm as shown in the last snapshot.

© Author(s) 2022

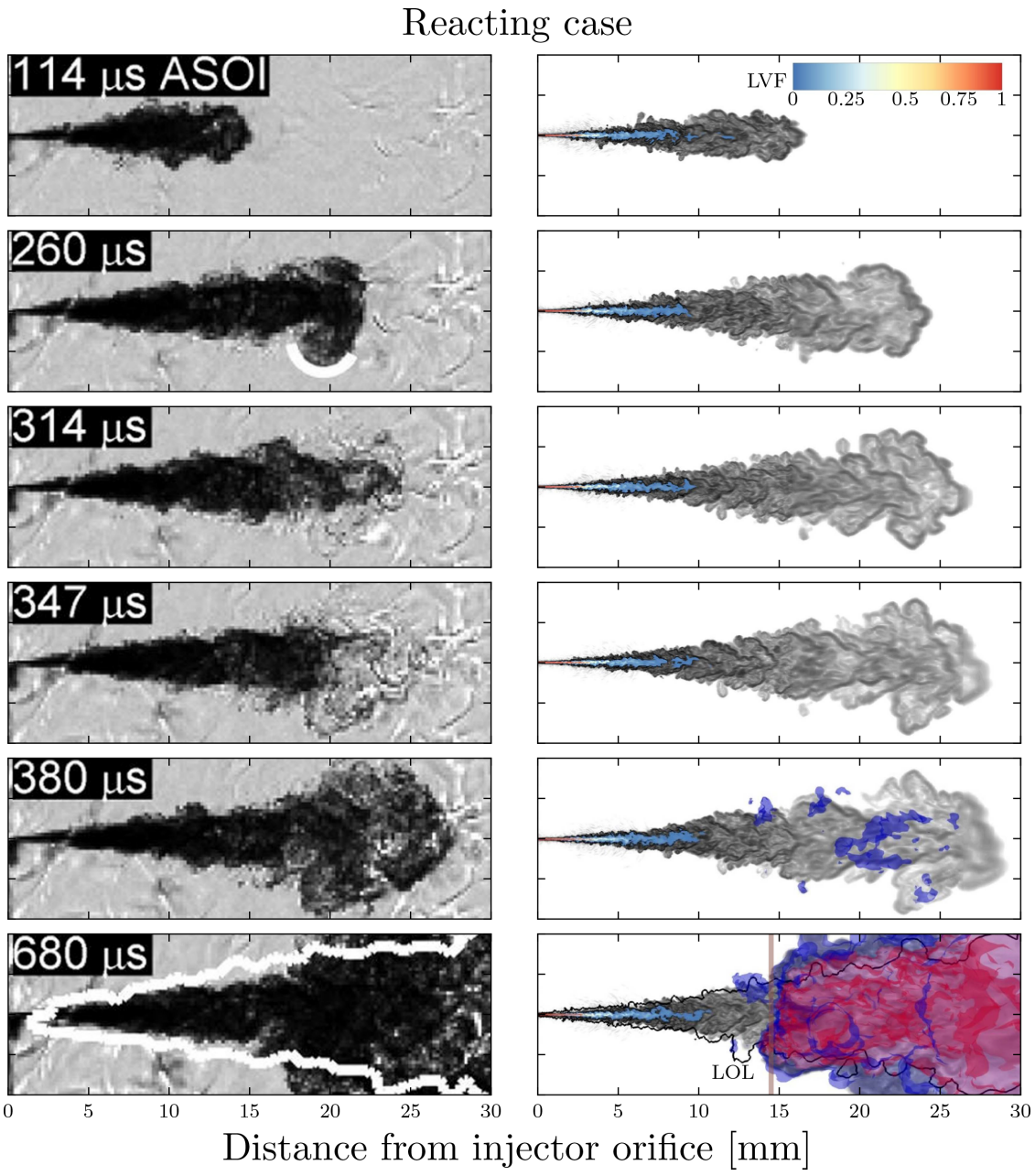


FIG. 10. Time sequence snapshots of reacting spray-A for experiment (schlieren images on the left[53]) and LES-MT (right). For the LES-MT, background contours of the density gradient are overprinted by liquid volume fraction contours in the two-phase region, and blue and red iso-surfaces for temperatures of 920 and 2000 K enclose the regions of low and high-temperature reactions. The flame liftoff length (LOL) is indicated in the last snapshot.

The reacting transcritical jet can be characterized by three important lengths scales: LPL, VPL, and LOL. Figure 11 shows the time evolution of these lengths for our LES-MT results and the experimental measurements.[54,55] For the LES-MT, LPL and VPL are computed by the method explained above for the non-reacting case. The LOL is computed as the minimum axial location where the temperature exceeds 1800 K. The uncertainty of the experimental measurements is indicated by the gray area around the dotted lines in Fig. 11. The numerically predicted and experimentally measured LPL evolution is in excellent agreement. The VPL evolution is in very good agreement up to about 40 mm and afterward the values predicted by the simulation are slightly higher than the experimental data. This is consistent with the results for the non-reacting case. The evolution of the flame LOL is again in excellent agreement with the experiment, even though

© Author(s) 2022

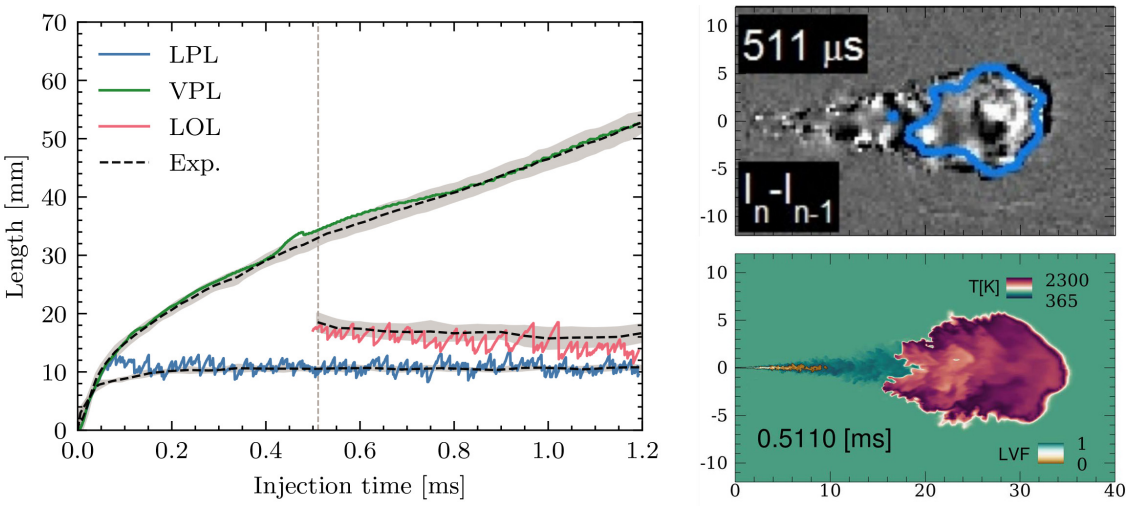


FIG. 11. Vapor and liquid penetration trajectories predicted by the LES-MT method and measured experimentally[54,55] for the reacting spray-A (left). The two right panels show an experimental schlieren image with highlighted flame boundaries along with an LES-MT temperature contour overprinted with the LVF at the same nominal time.

we use a highly reduced reaction mechanism for the simulation. In order to visualize the flame shape and volume, an experimental snapshot with highlighted high temperature boundaries is compared with the temperature contour plot for an LES-MT snapshot at the same time instant on the right side of Fig. 11. The numerical and experimental flame snapshots are in good qualitative agreement.

Figure 12 shows species mole fraction contours on a plane normal to the axial direction at $x = 18$ mm and $t = 590\ \mu$s, that is, at a

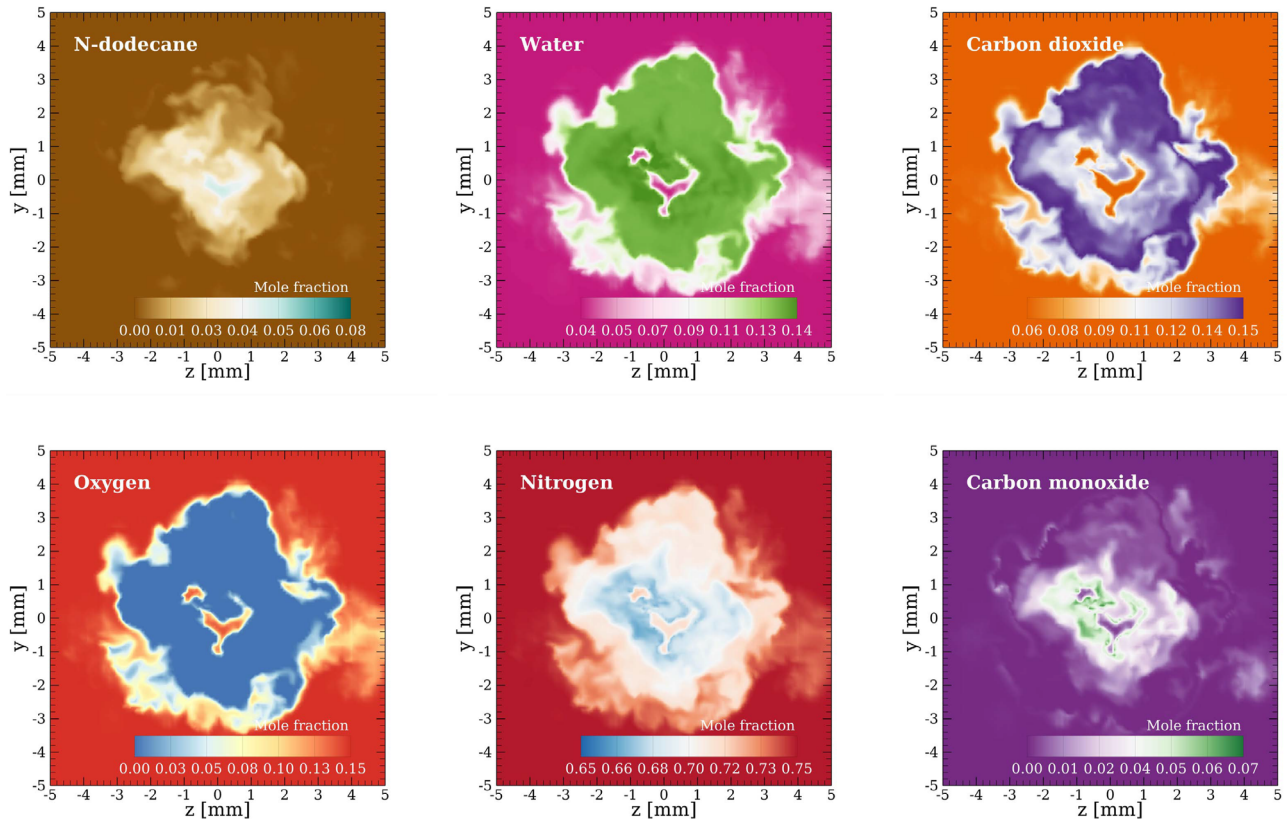


FIG. 12. Instantaneous snapshots of species mole fractions located at plane $x = 18$ mm at 590 μs ASOI in the reacting case.

© Author(s) 2022

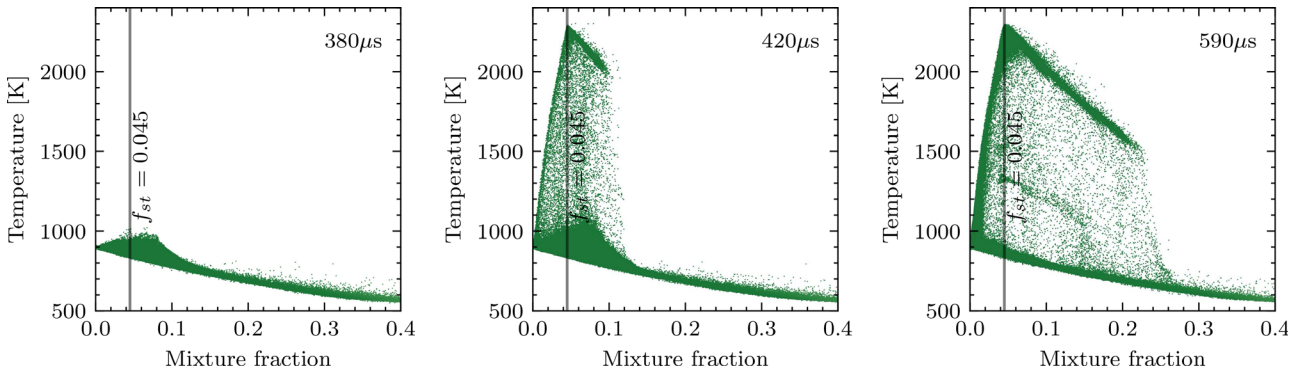


FIG. 13. Scatter plot of the temperature in mixture fraction space close to and after the ignition time.

distance larger than LOL of the developed flame. Accordingly, there exists no liquid phase at this location. The molar composition indicates partially premixed conditions of the fuel and environment even in the core of the reacting jet. The molar composition at the core is more close to the saturated vapor phase.

The auto-ignition process is illustrated in Fig. 13, where we show global scatter plots of the temperature in mixture fraction space at three different time instants. The first snapshot taken at 380 μs is representative for the very late pre-ignition state, where significant low-temperature reactions are occurring and the temperature is slowly increasing around the stoichiometric mixture fraction. The spatial distribution of these low-temperature kernels is shown in Fig. 10. The second snapshot is taken at 420 μs, that is, shortly after the auto-ignition time ($t \approx 400\,\mu$s). Several high-temperature flame kernels have been formed in regions with a stoichiometric mixture fraction, where enough radicals and intermediate species coexist. In the third snapshot at 590 μs, the ignition process is completed and has provided enough thermal energy for the propagation of the flame. We see that the high-temperature reactions are spreading into the fuel-rich regime.

V. DISCUSSION

The above-presented results of ECN spray-A simulations demonstrate the potential of LES-MT modeling for the accurate prediction of reacting and non-reacting turbulent multiphase fluid flows at transcritical pressures. The proposed LES-MT method is free from the main limitations of classical Lagrangian methods, which do not account for the solubility of real-fluid mixtures at elevated pressures and additionally may suffer from inaccurate density predictions if ideal-gas models are used, and Eulerian dense-gas (DG) models, which can become arbitrary inaccurate in the two-phase region (where they may predict negative pressures, e.g.). Moreover, high-pressure combustion typically initiates in low-temperature reacting zones in which the fluid state and transport properties deviate strongly from ideal-gas laws. Making ideal-gas assumptions, which is very common in combustion simulations, or the assumption of a dense-gas without accounting for local two-phase regions, can lead to large errors and uncertainties in transcritical combustion simulations. Furthermore, the LES-MT method provides the possibility of applying different reaction mechanisms in the liquid and vapor phases. Classical DG methods cannot make this distinction and have to apply the reaction mechanism on the overall composition, including possible condensates. For these reasons, we emphasize that real-fluid and phase-equilibrium effects should be considered in transcritical jets and flames. Doing so can yield very accurate predictions for the spreading angle, liquid penetration lengths, vapor penetration lengths, ignition delay time, and flame liftoff length, such as shown in Fig. 14 and discussed in Secs. I–IV.

The LES-MT method is accurate and calibration-free. To put its performance into perspective, we compare the results for the vapor and liquid penetration trajectories of spray-A computed with the present LES-MT method, LES-DG results of Hakim *et al.*,[9] results of the highly calibrated LES-LPT method of Gadalla *et al.*,[7] and the reference experiments[54,55] in Fig. 15. The figure shows the initial 0.2 ms of the transient startup during which we expect a similar behavior for the reacting and inert cases. Predictions of the current method are very close to the measurements for both liquid and vapor length.

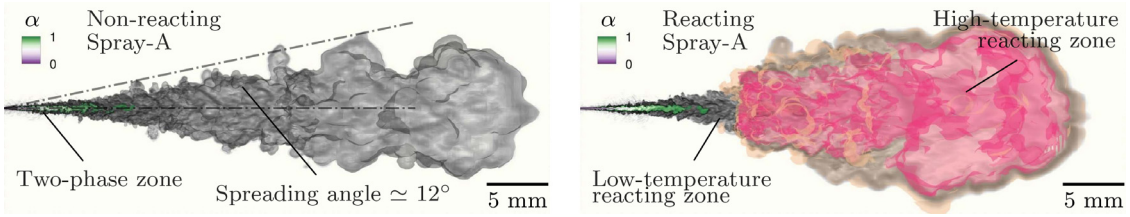


FIG. 14. Volume renderings at 800 μs after the start of transcritical injection of n-dodecane ($C_{12}H_{26}$ at 363 K) into a preheated chamber at 900 K without oxygen (left) and with oxygen (right) using a real-fluid finite-rate chemistry and multiphase thermodynamics models. The operating pressure is 60 bar, which exceeds the critical pressure of n-dodecane.

© Author(s) 2022

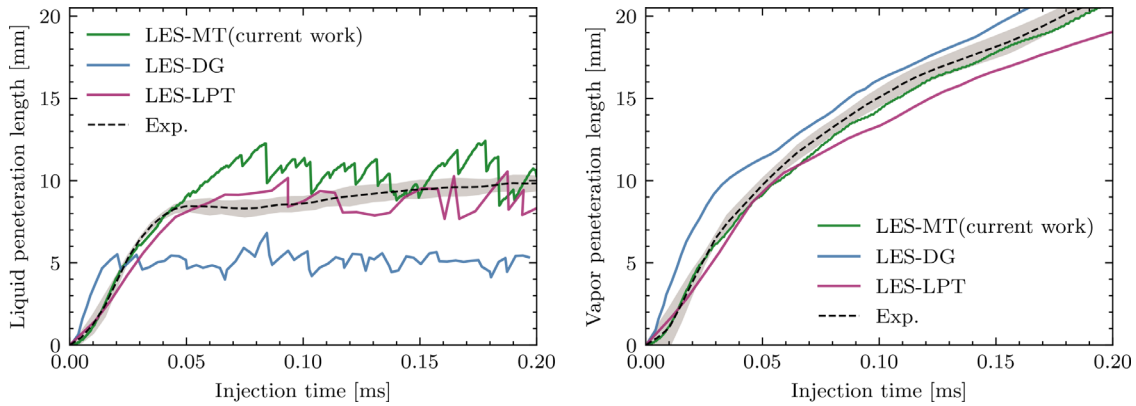


FIG. 15. Liquid- and vapor-penetration lengths for the LES-MT of the present paper, LES-DG of Hakim *et al.*,[9] and highly calibrated LES-LPT of Gadalla *et al.*[7] against the ECN spray-A experiment.[54,55]

Gadalla *et al.*[7] have calibrated the initial droplet size for their LES-LPT method in such a way that the liquid length is close to the experimental data. This calibration, however, apparently affected the vapor length prediction unfavorably. The single-phase DG method yields the least accurate prediction for this case. As the liquid phase boundaries are not directly predicted by the single-phase method, Hakim *et al.*[9] defined the boundary of the liquid regions via the mixture fraction value at which the density gradient peaks.

The major drawback of the LES-MT method might be the highly non-uniform computation costs, which limits the parallel scalability of flow solvers with domain decomposition methods. The wall-clock time for simulating 10 μs of the reacting spray, including time needed for writing snapshots every 0.5 μs, is approximately 8.5 h on 16 nodes with two Intel Xeon Gold 6248R CPU (24 cores at 3.00 GHz), which corresponds to approximately 6500 CPU h. On average, about 40% of the CPU time is used for evaluating the EOS and transport properties, and the majority of the rest is used for evaluating the reaction rates, the spatial derivatives of the Navier–Stokes equations, communication, and snapshot output.

Last but not least, it should be also mentioned that we have applied LES in a rather straightforward way without specifically addressing turbulence–combustion interactions other than by providing reasonable spatial and temporal resolution. The unresolved thermodynamic microstructure (SGS variations of pressure, temperature, and composition) has without doubt nonlinear effects on the resolved-scale solution,[57] and it seems reasonable to assume that transcritical multiphase flows are much stronger affected than ideal-gas or single-phase real-gas flows. Hence, the quantification of uncertainties resulting from the unresolved microstructure on the resolved pressure, temperature, and subgrid-scale terms are subject of our future studies.

VI. CONCLUSIONS

We have presented a real-fluid finite-rate chemistry multiphase thermodynamics model for the numerical simulation of transcritical vaporization, auto-ignition, and combustion of a cold or cryogenic fuel injected into a hot high-pressure environment. The methodology is based on solving the fully conservative form of the compressible multi-species Navier–Stokes equations along with real-fluid volumetric and caloric state equations. These state equations provide accurate real-fluid thermodynamic properties for multi-component fluids that can exist either in a single phase or undergo phase transitions during vaporization and condensation. Multiphase and real-gas effects are also considered in the finite-rate chemistry model, which we propose to be based on the fugacity or the molar specific volume function of the species.

The methodology has been demonstrated and validated for the transcritical reacting and non-reacting ECN spray-A. LES results obtained with the proposed thermodynamics models are in excellent agreement with experimental reference data for both cases. The time evolution of temperature in the mixture fraction space proves the existence of the low-temperature and high-temperature combustion stages in the auto-ignition process of spray-A that has been reported experimentally.

The very good agreement of auto-ignition time, flame liftoff length, and flame structure might be surprising because only a simple two-step reaction mechanism has been applied. However, one should note that Hakim's mechanism has been specifically calibrated for the considered flow conditions including low- and high-temperature ignition stages. In our LES, real-gas vapor–liquid equilibrium calculations accurately determine the saturated vapor composition, and this composition and the rate with which it mixes with the oxidizer determines when and where auto-ignition takes place.

ACKNOWLEDGMENTS

This paper is submitted as part of the themed issue "Development and Validation of Models for Turbulent Reacting Flows" in honor of Professor M. Pfitzner on the occasion of his retirement. The second author would like to thank Michael for motivating him to start working on this topic and for the very productive collaboration over many years.

This work is funded by The Netherlands Organization for Scientific Research (NWO) under Contract No. 680.91.082. Simulations have been performed on DelftBlue[58] at the Delft High Performance Computing Center (DHPC).

AUTHOR DECLARATIONS

Conflict of Interest

The authors have no conflicts to disclose.

© Author(s) 2022

Author Contributions

Mohamad Fathi: Data curation (lead); Formal analysis (lead); Investigation (lead); Methodology (equal); Software (equal); Validation (equal); Visualization (equal); Writing – original draft (lead); Writing – review and editing (supporting). **Stefan Hickel:** Conceptualization (lead); Funding acquisition (lead); Methodology (equal); Project administration (lead); Resources (lead); Software (equal); Supervision (lead); Writing – review and editing (lead). **Dirk Roekaerts:** Supervision (supporting); Writing – review and editing (supporting).

DATA AVAILABILITY

The data that support the findings of this study are available from the corresponding author upon reasonable request.

APPENDIX: SENSITIVITY TO GRID RESOLUTIONS

To evaluate the grid sensitivity of the presented numerical results, a grid convergence study is conducted by refining and coarsening the base grid. The finest grid has the minimum spacing of 6.84 μm, while the coarsest has 20.50 μm. By applying the same

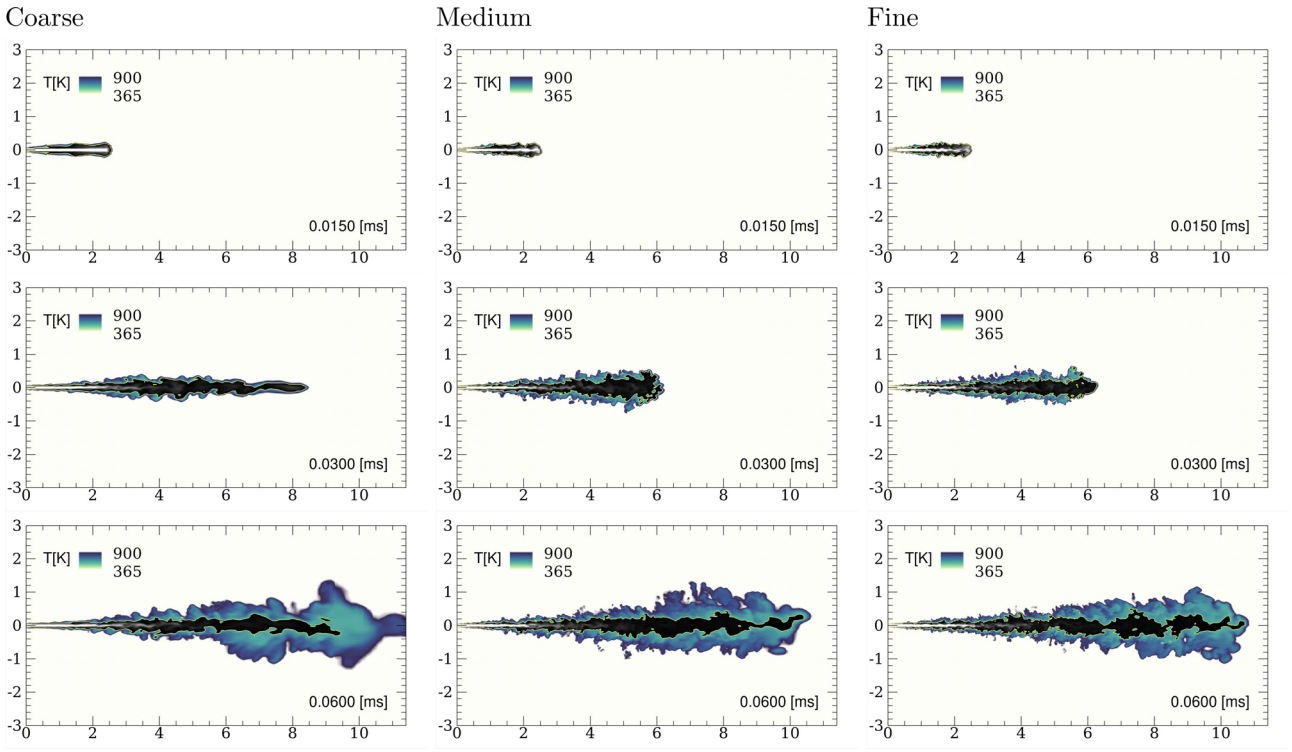


FIG. 16. Grid sensitivity of the temporal evolution of the temperature field superimposed by the LVF distribution from 1 to 0 printed white to black colors.

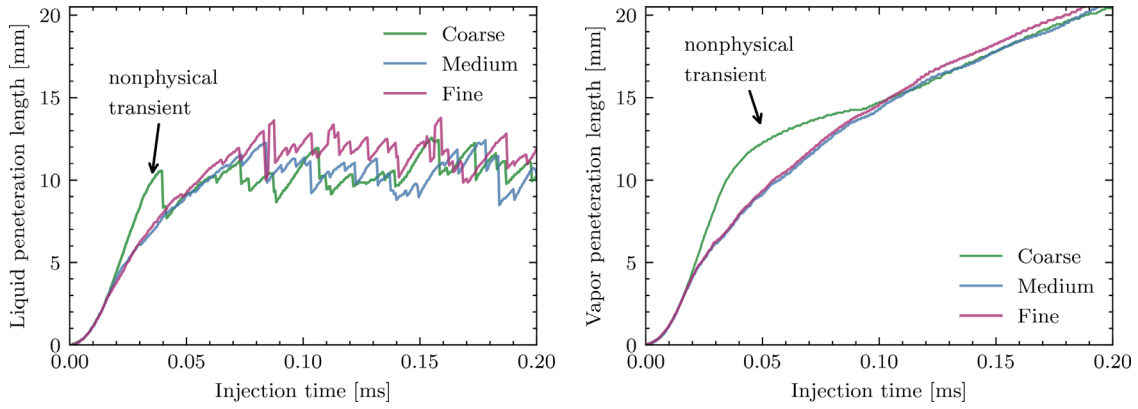


FIG. 17. Grid sensitivity of the liquid and vapor penetration trajectories.

© Author(s) 2022

local grid refinement procedure as used for the base grid (with 12.7×10^6 cells), we obtain a total cell number of about 1.2×10^6 for the coarse grid and 36.1×10^6 for finest grid.

Figure 16 visualizes the temporal evolution of the jet on the three grids. The results obtained on the medium and fine grid are almost indistinguishable, whereas a too rapid penetration and a different jet breakup topology are observed for the coarsest grid. Such a rapid nonphysical penetration was also reported by authors for too coarse meshes.[14] The main reason for this error is an insufficient number of cells in the radial direction resulting in extra momentum in the axial direction. The corresponding liquid and vapor penetration trajectories are shown in Fig. 17. Only negligible differences can be observed between the results obtained on the medium grid and on the fine grid.

REFERENCES

[1]W. Mayer, A. Schik, B. Vielle, C. Chauveau, I. Gokalp, D. Talley, and R. Woodward, "Atomization and breakup of cryogenic propellants under high-pressure subcritical and supercritical conditions," J. Propul. Power **14**, 835–842 (1998).

[2]G. Singla, P. Scouflaire, C. Rolon, and S. Candel, "Transcritical oxygen/transcritical or supercritical methane combustion," Proc. Combust. Inst. **30**, 2921–2928 (2005).

[3]J. Gimeno, G. Bracho, P. Martí-Aldaraví, and J. Peraza, "Experimental study of the injection conditions influence over n-dodecane and diesel sprays with two ECN single-hole nozzles. I. Inert atmosphere," Energy Convers. Manage. **126**, 1146–1156 (2016).

[4]R. Payri, F. J. Salvador, J. Gimeno, and J. Peraza, "Experimental study of the injection conditions influence over n-dodecane and diesel sprays with two ECN single-hole nozzles. II. Reactive atmosphere," Energy Convers. Manage. **126**, 1157–1167 (2016).

[5]Y. Pei, S. Som, E. Pomraning, P. Senecal, S. Skeen, J. Manin, and L. Pickett, "Large eddy simulation of a reacting spray flame with multiple realizations under compression ignition engine conditions," Combust. Flame **162**, 4442–4455 (2015).

[6]H. Kahila, A. Wehrfritz, O. Kaario, M. Ghaderi Masouleh, N. Maes, B. Somers, and V. Vuorinen, "Large-eddy simulation on the influence of injection pressure in reacting spray A," Combust. Flame **191**, 142–159 (2018).

[7]M. Gadalla, J. Kannan, B. Tekgül, S. Karimkashi, O. Kaario, and V. Vuorinen, "Large-eddy simulation of ECN spray A: Sensitivity study on modeling assumptions," Energies **13**, 3360 (2020).

[8]G. Lacaze, A. Misdariis, A. Ruiz, and J. Oefelein, "Analysis of high-pressure diesel fuel injection processes using LES with real-fluid thermodynamics and transport," Proc. Combust. Inst. **35**, 1603–1611 (2015).

[9]L. Hakim, G. Lacaze, and J. Oefelein, "Large eddy simulation of autoignition transients in a model diesel injector configuration," SAE Int. J. Fuels Lubr. **9**, 165–176 (2016).

[10]L. Jofre and J. Urzay, "Transcritical diffuse-interface hydrodynamics of propellants in high-pressure combustors of chemical propulsion systems," Prog. Energy Combust. Sci. **82**, 100877 (2021).

[11]P. Ma, H. Wu, D. Banuti, and M. Ihme, "On the numerical behavior of diffuse-interface methods for transcritical real-fluids simulations," Int. J. Multiphase Flow **113**, 231–249 (2019).

[12]L. Ricart, R. Reltz, and J. Dec, "Comparisons of diesel spray liquid penetration and vapor fuel distributions with in-cylinder optical measurements," J. Eng. Gas Turbines Power **122**, 588–595 (2000).

[13]L. Qiu and R. Reitz, "An investigation of thermodynamic states during high-pressure fuel injection using equilibrium thermodynamics," Int. J. Multiphase Flow **72**, 24–38 (2015).

[14]J. Matheis and S. Hickel, "Multi-component vapor-liquid equilibrium model for LES of high-pressure fuel injection and application to ECN spray A," Int. J. Multiphase Flow **99**, 294–311 (2018).

[15]P. Tudisco and S. Menon, "Analytical framework for real-gas mixtures with phase-equilibrium thermodynamics," J. Supercrit. Fluids **164**, 104929 (2020).

[16]J. Matheis, H. Müller, S. Hickel, and M. Pfitzner, "Large-eddy simulation of cryogenic jet injection at supercritical pressures," in *High-Pressure Flows for Propulsion Applications*, edited by J. Bellan (American Institute of Aeronautics and Astronautics, 2020), pp. 531–570.

[17]J. Matheis and S. Hickel, "Multi-component vapor-liquid equilibrium model for LES and application to ECN spray A," in *Proceedings of the Center for Turbulence Research 2016 Summer Program* (Stanford University, 2016), p. 25.

[18]S. Yang, P. Yi, and C. Habchi, "Real-fluid injection modeling and LES simulation of the ECN spray A injector using a fully compressible two-phase flow approach," Int. J. Multiphase Flow **122**, 103145 (2020).

[19]P. Koukouvinis, A. Vidal-Roncero, C. Rodriguez, M. Gavaises, and L. Pickett, "High pressure/high temperature multiphase simulations of dodecane injection to nitrogen: Application on ECN spray-A," Fuel **275**, 117871 (2020).

[20]L. Hakim, G. Lacaze, M. Khalil, K. Sargsyan, H. Najm, and J. Oefelein, "Probabilistic parameter estimation in a 2-step chemical kinetics model for n-dodecane jet autoignition," Combust. Theor. Modell. **22**, 446–466 (2018).

[21]G. Kogekar, C. Karakaya, G. Liskovich, M. Oehlschlaeger, S. DeCaluwe, and R. Kee, "Impact of non-ideal behavior on ignition delay and chemical kinetics in high-pressure shock tube reactors," Combust. Flame **189**, 1–11 (2018).

[22]G. Soave, "Equilibrium constants from a modified Redlich-Kwong equation of state," Chem. Eng. Sci. **27**, 1197–1203 (1972).

[23]D.-Y. Peng and D. Robinson, "A new two-constant equation of state," Ind. Eng. Chem. Fundam. **15**, 59–64 (1976).

[24]P. Ma, L. Bravo, and M. Ihme, "Supercritical and transcritical real-fluid mixing in diesel engine applications," in *Proceedings of the Center for Turbulence Research 2014 Summer Program* (Stanford University, 2014), p. 99.

[25]J. Bellan, "Direct numerical simulation of a high-pressure turbulent reacting temporal mixing layer," Combust. Flame **176**, 245–262 (2017).

[26]X. Wang, H. Huo, U. Unnikrishnan, and V. Yang, "A systematic approach to high-fidelity modeling and efficient simulation of supercritical fluid mixing and combustion," Combust. Flame **195**, 203–215 (2018).

[27]C. Traxinger, J. Zips, and M. Pfitzner, "Single-phase instability in non-premixed flames under liquid rocket engine relevant conditions," J. Propul. Power **35**, 675–689 (2019).

[28]J. Matheis, H. Müller, C. Lenz, M. Pfitzner, and S. Hickel, "Volume translation methods for real-gas computational fluid dynamics simulations," J. Supercrit. Fluids **107**, 422–432 (2016).

[29]M. Cismondi and J. Mollerup, "Development and application of a three-parameter RK-PR equation of state," Fluid Phase Equilib. **232**, 74–89 (2005).

[30]S. K. Kim, H. S. Choi, and Y. Kim, "Thermodynamic modeling based on a generalized cubic equation of state for kerosene/LOx rocket combustion," Combust. Flame **159**, 1351–1365 (2012).

[31]M. Fathi and S. Hickel, "Rapid multi-component phase-split calculations using volume functions and reduction methods," AIChE J. **67**, e17174 (2021).

[32]M. Michelsen and J. Mollerup, *Thermodynamic Modelling: Fundamentals and Computational Aspects* (Tie-Line Publications, 2004).

[33]S. Hickel, C. Egerer, and J. Larsson, "Subgrid-scale modeling for implicit large eddy simulation of compressible flows and shock-turbulence interaction," Phys. Fluids **26**, 106101 (2014).

[34]B. Poling, J. Prausnitz, and J. O'Connell, *The Properties of Gases and Liquids* (McGraw-Hill Companies, 2001).

[35]R. Krishna and J. van Baten, "Describing diffusion in fluid mixtures at elevated pressures by combining the Maxwell–Stefan formulation with an equation of state," Chem. Eng. Sci. **153**, 174–187 (2016).

[36]E. W. Lemmon and M. L. Huber, "Thermodynamic properties of n-dodecane," Energy Fuels **18**, 960–967 (2004).

[37]J. Gross and G. Sadowski, "Perturbed-chain saft: An equation of state based on a perturbation theory for chain molecules," Ind. Eng. Chem. Res. **40**, 1244–1260 (2001).

[38]S. Aparicio-Martinez and K. Hall, "Thermodynamic properties of light synthetic natural gas mixtures using the RK-PR cubic equation of state," Ind. Eng. Chem. Res. **45**, 3684–3692 (2006).

[39]A. Burcat and R. Branko, "Third millennium ideal gas and condensed phase thermochemical database for combustion with updates from active thermochemical tables," Technical Report No. TAE960 (Argonne National Laboratory (ANL), Argonne, IL, 2005).

© Author(s) 2022

[40]J. Mikyška and A. Firoozabadi, "A new thermodynamic function for phase-splitting at constant temperature, moles, and volume," AIChE J. **57**, 1897–1904 (2011).
[41]D. V. Nichita and A. Graciaa, "A new reduction method for phase equilibrium calculations," Fluid Phase Equilib. **302**, 226–233 (2011).
[42]J. Gmehling, M. Kleiber, B. Kolbe, and J. Rarey, *Chemical Thermodynamics for Process Simulation* (Wiley Online Library, 2019).
[43]F. Diegelmann, S. Hickel, and N. A. Adams, "Shock Mach number influence on reaction wave types and mixing in reactive shock-bubble interaction," Combust. Flame **174**, 85–99 (2016).
[44]S. Hickel, N. A. Adams, and J. A. Domaradzki, "An adaptive local deconvolution method for implicit LES," J. Comput. Phys. **213**, 413–436 (2006).
[45]H. Müller, C. A. Niedermeier, J. Matheis, M. Pfitzner, and S. Hickel, "Large-eddy simulation of nitrogen injection at trans- and supercritical conditions," Phys. Fluids **28**, 015102 (2016).
[46]H. Müller, M. Pfitzner, J. Matheis, and S. Hickel, "Large-eddy simulation of coaxial LN2/GH2 injection at trans- and supercritical conditions," J. Propul. Power **32**, 46–56 (2016).
[47]G. van Albada, B. van Leer, and W. W. Roberts, "A comparative study of computational methods in cosmic gas dynamics," in *Upwind and High-Resolution Schemes* (Springer, Berlin, Heidelberg, 1997), pp. 95–103.
[48]P. Brown, G. Byrne, and A. Hindmarsh, "VODE: A variable-coefficient ODE solver," SIAM J. Sci. Stat. Comput. **10**, 1038–1051 (1989).
[49]S. Gottlieb and C.-W. Shu, "Total variation diminishing Runge-Kutta schemes," Math. Comput. **67**, 73–85 (1998).
[50]L. Pickett, C. Genzale, G. Bruneaux, L.-M. Malbec, L. Hermant, C. Christiansen, and J. Schramm, "Comparison of diesel spray combustion in different high-temperature, high-pressure facilities," SAE Int. J. Engines **3**, 156–181 (2010).
[51]L. Hakim, G. Lacaze, M. Khalil, H. Najm, and J. Oefelein, "Modeling auto-ignition transients in reacting diesel jets," J. Eng. Gas Turbines Power **138**, 112806 (2016).
[52]K. Narayanaswamy, P. Pepiot, and H. Pitsch, "A chemical mechanism for low to high temperature oxidation of n-dodecane as a component of transportation fuel surrogates," Combust. Flame **161**, 866–884 (2014).
[53]S. Skeen, J. Manin, and L. Pickett, "Simultaneous formaldehyde PLIF and high-speed schlieren imaging for ignition visualization in high-pressure spray flames," Proc. Combust. Inst. **35**, 3167–3174 (2015).
[54]L. Pickett and J. Abraham, "Computed and measured fuel vapor distribution in a diesel spray," Atomization Sprays **20**, 241–250 (2010).
[55]P. Lillo, L. Pickett, H. Persson, O. Andersson, and S. Kook, "Diesel spray ignition detection and spatial/temporal correction," SAE Int. J. Engines **5**, 1330 (2012).
[56]C. Genzale, C. Idicheria, J. Manin, L. Pickett, D. Siebers, and M. Musculus, "Relationship between diesel fuel spray vapor penetration/dispersion and local fuel mixture fraction," SAE Int. J. Engines **4**, 764–799 (2011).
[57]U. Unnikrishnan, J. C. Oefelein, and V. Yang, "Subgrid modeling of the filtered equation of state with application to real-fluid turbulent mixing at supercritical pressures," Phys. Fluids **34**, 065112 (2022).
[58]Delft High Performance Computing Centre (DHPC), DelftBlue Supercomputer (Phase 1), 2022, https://www.tudelft.nl/dhpc/ark:/44463/DelftBluePhase1.

© Author(s) 2022